Initial Circulation and Peak Vorticity Behavior of Vortices Shed From Airfoil Vortex Generators

Bruce J. Wendt
Modern Technologies Corporation, Middleburg Heights, Ohio

Since its founding, NASA has been dedicated to the advancement of aeronautics and space science. The NASA Scientific and Technical Information (STI) Program Office plays a key part in helping NASA maintain this important role.

The NASA STI Program Office is operated by Langley Research Center, the Lead Center for NASA's scientific and technical information. The NASA STI Program Office provides access to the NASA STI Database, the largest collection of aeronautical and space science STI in the world. The Program Office is also NASA's institutional mechanism for disseminating the results of its research and development activities. These results are published by NASA in the NASA STI Report Series, which includes the following report types:

- TECHNICAL PUBLICATION. Reports of completed research or a major significant phase of research that present the results of NASA programs and include extensive data or theoretical analysis. Includes compilations of significant scientific and technical data and information deemed to be of continuing reference value. NASA's counterpart of peer-reviewed formal professional papers but has less stringent limitations on manuscript length and extent of graphic presentations.

- TECHNICAL MEMORANDUM. Scientific and technical findings that are preliminary or of specialized interest, e.g., quick release reports, working papers, and bibliographies that contain minimal annotation. Does not contain extensive analysis.

- CONTRACTOR REPORT. Scientific and technical findings by NASA-sponsored contractors and grantees.

- CONFERENCE PUBLICATION. Collected papers from scientific and technical conferences, symposia, seminars, or other meetings sponsored or cosponsored by NASA.

- SPECIAL PUBLICATION. Scientific, technical, or historical information from NASA programs, projects, and missions, often concerned with subjects having substantial public interest.

- TECHNICAL TRANSLATION. English-language translations of foreign scientific and technical material pertinent to NASA's mission.

Specialized services that complement the STI Program Office's diverse offerings include creating custom thesauri, building customized data bases, organizing and publishing research results . . . even providing videos.

For more information about the NASA STI Program Office, see the following:

- Access the NASA STI Program Home Page at *http://www.sti.nasa.gov*

- E-mail your question via the Internet to help@sti.nasa.gov

- Fax your question to the NASA Access Help Desk at 301–621–0134

- Telephone the NASA Access Help Desk at 301–621–0390

- Write to:
  NASA Access Help Desk
  NASA Center for AeroSpace Information
  7121 Standard Drive
  Hanover, MD 21076

NASA/CR—2001-211144

Initial Circulation and Peak Vorticity Behavior of Vortices Shed From Airfoil Vortex Generators

Bruce J. Wendt
Modern Technologies Corporation, Middleburg Heights, Ohio

National Aeronautics and
Space Administration

Glenn Research Center

August 2001

Acknowledgments

INITIAL CIRCULATION AND PEAK VORTICITY BEHAVIOR OF VORTICES SHED FROM AIRFOIL VORTEX GENERATORS

B.J. Wendt*
Modern Technologies Corporation
Middleburg Heights, Ohio 44130

Abstract

An extensive parametric study of vortices shed from airfoil vortex generators has been conducted to determine the dependence of initial vortex circulation and peak vorticity on elements of the airfoil geometry and impinging flow conditions. These elements include the airfoil angle-of-attack, chord-length, span, aspect ratio, local boundary layer thickness, and free-stream Mach number. In addition, the influence of airfoil-to-airfoil spacing on the circulation and peak vorticity has been examined for pairs of co-rotating and counter-rotating vortices.

The vortex generators were symmetric airfoils having a NACA-0012 cross-sectional profile. These airfoils were mounted either in isolation, or in pairs, on the surface of a straight pipe. The turbulent boundary layer thickness to pipe radius ratio was about 17 percent. The circulation and peak vorticity data were derived from cross-plane velocity measurements acquired with a seven-hole probe at one chord-length downstream of the airfoil trailing edge location.

The circulation is observed to be proportional to the free-stream Mach number, the angle-of-attack, and the span-to-boundary layer thickness ratio. With these parameters held constant, the circulation is observed to fall off in monotonic fashion with increasing airfoil aspect ratio. The peak vorticity is also observed to be proportional to the free-stream Mach number, the airfoil angle-of-attack, and the span-to-boundary layer thickness ratio. Unlike circulation, however, the peak vorticity is observed to increase with increasing aspect ratio, reaching a peak value at an aspect ratio of about 2.0 before falling off again at higher values of aspect ratio. Co-rotating vortices shed from closely-spaced pairs of airfoils have values of circulation and peak vorticity under those values found for vortices shed from isolated airfoils of the same geometry. Conversely, counter-rotating vortices show enhanced values of circulation and peak vorticity when compared to values obtained in isolation.

The circulation may be accurately modeled with an expression based on Prandtl's relationship between finite airfoil circulation and airfoil geometry. A correlation for the peak vorticity has been derived from a conservation

relationship equating the moment at the airfoil tip to the rate of angular momentum production of the shed vortex, modeled as a Lamb (ideal viscous) vortex. This technique provides excellent qualitative agreement to the observed behavior of peak vorticity for low aspect ratio airfoils typically used as vortex generators.

Introduction

Modern design characteristics of aircraft engine inlets, diffusers, and associated ducting include large amounts of streamwise curvature coupled with rapid axial variations in cross-sectional area. The flow performance of these components is degraded by the development of strong secondary flows and boundary layer separations. Surface mounted vortex generators are an effective means of alleviating these problems. Recent experimental work at the NASA Glenn Research Center in Cleveland, Ohio has explored the strategy of using vortex generator induced flows to counter deleterious secondary flow development and boundary layer separation inside diffusing S-ducts of various geometries.[1-5] Dramatic improvements in exit plane total pressure recovery and flow distortion have been demonstrated. Figures 1 and 2 provide an example.

The duct in Figure 1 was a highly offset S-duct having a "biconvex" aperture for an inflow (or throat) cross-section. This biconvex shape transitioned to a circular engine face of diameter D over an axial distance L of about 2.5D. The area ratio (throat to engine face cross-sectional area) was about 1.2. This duct geometry represented a subsonic inlet proposed for use in a compact unmanned combat aircraft where stealth considerations required large amounts of streamwise curvature to screen the engine face from all lines of sight through the inlet cowl-plane aperture. Figure 2 illustrates the experimentally-determined profiles of total pressure at the engine face for both the baseline duct and the duct with two arrays of surface-mounted vane vortex generators. The throat Mach number was 0.65 and the upstream reference total pressure was atmospheric. Figure 1 indicates the approximate axial location where the vortex generators were applied.[4] The numbers given in Figure 2 indicate a 5% improvement in total pressure recovery and a 56% drop in circumferential distortion intensity. That such dramatic improvements can be obtained in this highly

---

*NASA Resident Research Associate at Glenn Research Center.

contoured and three-dimensional diffuser is strong testament to the potential flow control available in simple vortex generator vanes *when used following the strategy of secondary flow management*. Formal elements of this strategy have recently been developed computationally by Anderson and Gibb[6-8] using the RNS3D code, a parabolized Navier-Stokes solver. The experimental results given in Figure 2 were initially designed computationally using the Falcon code, a Reynolds-averaged Navier-Stokes solver[9] in a procedure detailed in Reference 4. Common to both the RNS3D and Falcon flow solvers is the manner in which the vortex generator flow control is modeled. The vortex generators are not modeled as part of the flow surface grid, rather they are represented by modeling the convective influence of the vortex shed from each vortex generator at an "initial" location in the flow field grid downstream of where the airfoils would be located in a corresponding experimental arrangement. The basis of this convective influence is found in the helical pattern of swirling flow; either the secondary velocity or streamwise vorticity can be used.

The advantage to modeling the secondary velocity or streamwise vorticity distribution induced by the vortex generator is that a simple exponential expression accurately captures the secondary velocity or streamwise vorticity distribution of the shed vortex. To demonstrate this, consider Figure 3. Figure 3 illustrates the secondary velocity field of an embedded vortex (data on the left, model on the right) shed from an airfoil vortex generator. This vortex generator was one of 12 symmetrically placed vortex generators spanning the inside circumference of a straight pipe. The data was acquired in the cross-plane one chord-length downstream of the vortex generators. The model was constructed from a summation of 24 terms (12 embedded vortices plus 12 image vortices), each term being proportional to the expression:[10, 25]

$$\frac{\Gamma_i}{2\pi r_i^2}\left[1-\exp\left(\frac{-\pi\,\omega_{max}^i}{\Gamma_i}r_i^2\right)\right] \qquad (1)$$

where Γ_i is the measured initial circulation of the ith vortex or image, ω_{max}^i is the measured initial peak vorticity, and r_i is the distance from the cross-plane grid point to the center of vortex i. The parameters Γ_i, ω_{max}^i, and the center location of the vortex are known as "vortex descriptors" following the work of Russell Westphal.[11] Any such model requires a description of the vortex strength (here Γ_i) and concentration (here ω_{max}^i, but viscous core radius R_i is another option). The model above is based on the classical "ideal viscous" or Lamb vortex. The axial location where the model is placed (the initial location mentioned earlier) is the position at which the formative or "roll-up" processes of the vortex are complete. Circulation and peak vorticity have reached maximum values here and further downstream development leads to decay in both quantities. Previous studies[10,12] have indicated the initial location occurs about

one chord-length downstream of the airfoil trailing edge. From this point on, the terms Γ and ω_{max} will represent these initial values of the vortex descriptors.

Many studies have demonstrated the remarkable similarities between the Lamb-based model and the cross-plane structure of embedded vortices shed from various types of vortex generators. Pauley and Eaton[13] demonstrated this in a study of delta wing vortex generators, Wendt *et al.*[14] in a study of blade-type vortex generators, Wendt and Hingst[15] for low-profile wishbone vortex generators, and more recently, Wendt *et al.*[10,12,16] on symmetric airfoil vortex generators.

To complete the modeling of a vortex generator we must show how the descriptors of the model vortex depend on the geometry of the vortex generator, the influence of neighboring vortex generators, and the impinging flow conditions. For airfoil vortex generators we might express this dependence as:

$$\Gamma = \Gamma\left(c, h, \alpha, profile, s, \partial, M, \text{Re}, ...\right)$$
$$\omega_{max} = \omega_{max}\left(c, h, \alpha, profile, s, \partial, M, \text{Re}, ...\right) \qquad (2)$$

where "profile" refers to the shape of the airfoil cross-section, c is the chord-length, h is the span (the airfoil dimension normal to the duct flow surface), α the angle-of-attack, s a spacing variable representative of the distance between vortex generators in an array formation, δ the boundary layer thickness, M the free-stream Mach number, and Re represents the Reynolds number. The mathematical descriptions of vortex generators in use at the present time only crudely approximate the functional dependence indicated in Equation (2). As a means of improving current vortex generator models this study was undertaken to examine the effect of vortex generator geometry, spacing, and impinging flow conditions for one type of symmetric airfoil vortex generator (NACA-0012). This paper reports the results of a series of experimental tests covering a range of vortex generator aspect ratio ($\sim h/c$), h/δ, α, and M. Spacing effects were examined by considering co-rotating and counter-rotating pairs of vortex generators. The vortex generators were mounted either in isolation, in pairs, or (in one instance) in a symmetric counter-rotating array spanning the full circumference of the pipe. Duct or pipe flow conditions were subsonic with a nominal boundary layer thickness to pipe diameter ratio, $\delta/D \approx 0.09$. Three dimensional mean flow velocity data were acquired in a cross-plane grid always located one chord-length downstream of the vortex generator trailing edge(s). This was done using a rake of seven-hole probes or a single seven-hole probe tip. This work represents an extension of the work conducted in Reference 12. In Reference 12 a total of 14 test cases were considered. An additional 88 test cases are considered (and fully illustrated) in this report. Comparisons of the experimental results with expressions derived from inviscid airfoil theory and a conservation relationship are conducted to establish the

Γ and ω_{max} dependence on airfoil geometry and impinging flow conditions. Closed-form functional relationships are obtained for this limited set of parameters and are described here.

Facilities and Procedures

Test Facility

This study was conducted in the Internal Fluid Mechanics Facility (IFMF) of NASA Glenn. The IFMF is a subsonic facility designed to investigate a variety of duct flow phenomena. The facility, as it is configured for this test, is illustrated in Figure 4. Air is supplied from the surrounding test cell to a large settling chamber containing a honeycomb flow straightener and screens. At the downstream end of the settling chamber the airstream is accelerated through a contraction section (having a cross-sectional area reduction of 59 to 1) to the test section. The test section duct consists of a straight circular pipe of inside diameter $D = 20.4$ cms. After exiting the test section duct, the airstream enters a short conical diffuser and is routed to a discharge plenum, which is continuously evacuated by the laboratory's central exhauster facilities. The Mach number range in the test section duct is between 0.20 and 0.80 with corresponding Reynolds numbers (based on pipe diameter) between 1.0 and 4.0 million. Mass flows are between 3 and 7 kgs/sec. More information on the design and operation of the IFMF may be found in the report of Porro et al.[17]

Research Instrumentation and Test Parameters

Figure 5 is a detailed illustration of the various test section components.

A short section of straight pipe (labeled "inlet pipe" in Figure 5) connects the exit of the facility contraction to the duct segment containing the vortex generator airfoil(s). Static pressure taps located on the surface of the inlet pipe allowed the nominal core Mach number in the test section to be set and monitored.

The duct portion containing the vortex generator airfoil(s) was referred to as the "vortex generator duct." The inside surface of the vortex generator duct (and hence the attached vortex generator) could be rotated about an axis coinciding with the test section centerline. Full (360°) rotation was possible. The rotation was driven by a motor and gear located in an airtight box above the vortex generator duct.

Single-Airfoil Vortex Generator

A typical single-airfoil vortex generator is illustrated in Figure 6. These vortex generators consisted of an airfoil-shaped blade (with a NACA-0012 profile) mounted perpendicular to the surface of a base plug. The surface of the base plug was contoured to the inside radius of the vortex generator duct. Both blade and plug were machined from an aluminum alloy using a wire-cutting (electric discharge machining) process. Table 1 provides the detailed geometry of all single-airfoil vortex generators used in this study.

Airfoil Array Configurations and the Double-Airfoil Vortex Generator

A single circumferential row of vortex generator mounting locations was contained in the vortex generator duct as illustrated in Figure 5. Figure 7 illustrates a cross-section of the rotating flow surface (inner cylinder) of the vortex generator duct in the vicinity of the vortex generator mounting locations. Twelve mounting locations were spaced 30° apart and thus covered the entire inside circumference of the pipe. The spacing between vortex generators in array configurations is given in nondimensional form, s/c, where s is the arc-length (measured along the flow surface) between vortex generators at the mid-chord location, from profile centerpoint to profile centerpoint. For test conditions considering the variation in pipe core Mach number, vortex generators were tested in a full counter-rotating array (12 airfoils spaced 30° apart at the mid-chord position on the airfoil). Table 1 provides the geometry of the single-airfoil vortex generators used in this array. As indicated in Figure 7, an additional 4 mounting locations created a 120° sector with 9 mounting locations 15° apart. This provided for two spacing conditions (15 and 30°) for vortex generators tested in pairs. Table 1 provides the geometry of the single-airfoil vortex generators used in this manner.

Airfoils with a chord-length of 1.355 cms were constructed in the two-to-a-plug configurations illustrated in Figure 8. Figure 8 diagrams the three different possibilities: co-rotating, counter-rotating up, and counter-rotating down pairs. The "up" and "down" designations refer to the direction of secondary flow occurring between the vortex pair shed from the vortex generator (e.g., a pair of vortices produced by a counter-rotating up vortex generator has secondary flow, between cores, directed away from the flow surface). Table 2 provides the geometry of all double-airfoils tested. Note that the description of vortex generator pairings appropriate for double-airfoils (i.e., co-rotating, counter-rotating up, etc.) apply to pairs created with single airfoils as well (Table 1).

Instrumentation

The coordinate system used in this study originated in the vortex generator duct. $z = 0$ coincided with the trailing edge of the vortex generator or vortex generator array. All surveys conducted in this study were carried out in the r-θ cross-plane at an axial location $z = 1$ chord-length.

The duct segment downstream of the vortex generator duct is stationary (non-rotating). This test section segment is referred to as the "instrumentation duct" in Figure 5. The flow field measurements are acquired in this duct (at the 12 o'clock position) through the use of either a radially-actuated rake probe (with 4 seven-hole probe tips, as in Figure 5) or a single radially-actuated seven-hole probe tip.

These probe tips were calibrated in accordance with the procedure outlined by Zilliac.[18] The flow angle range covered in calibration was ±40° in both pitch and yaw. Uncertainty in flow angle measurement was ±0.7° in either pitch or yaw, for flow angle magnitude below 35° (pitch and yaw flow angle magnitude rarely exceeded 35° in this study). The corresponding uncertainty in velocity magnitude was approximately ±1% of the core velocity, v_{zc}.

Figure 9 is a detailed sketch of the single seven-hole probe tip. The tip could slide in the z coordinate, to be pinned at any one of seven different locations (for the seven different airfoil chord-lengths examined in this study). The probe tip was always located 1 chord-length downstream of the vortex generator, or vortex generator array, trailing edge. The axially-fixed rake probe was used only if the vortex generators had a chord-length of 4.064 cms.

To acquire data in the r-θ cross-plane the rake probe, or single probe, was actuated over a certain radial segment along the vertical line extending from duct wall to pipe center. The vortex generator duct flow surface and vortex generator(s) were then rotated an increment in circumferential position, $\Delta\theta$, and the radial survey repeated. In this manner the rake probe would acquire pie-shaped pieces of the flow field, and the single probe would acquire ring-segment-shaped pieces. The circumferential and radial extent of the survey grid was determined by the requirement that the viscous core of the vortex be fully captured. This allowed the calculation of Γ and ω_{max} as explained below. In most cases, the circumferential extent of the survey grid was about 15°, and the radial extent was about 0.700 cms. Grid resolution was $\Delta\theta = 1°$ and $\Delta r = 1.3$ mm.

Experimental Results

Tables 3-6 and Figures 11-22 summarize and illustrate the results of this study. Tables 3-6 list the test conditions for every flow field result illustrated in Figures 11-22, and tabulate the vortex descriptors determined for each captured vortex. The pertinent airfoil geometry, airfoil array configuration, and vortex descriptors are also included on Figures 11-22. The figures illustrate a total of 90 surveyed flow fields. Each illustrated flow field consists of a cross-plane vector plot of secondary velocity (on the left hand side), a contour plot of primary velocity ratio (in the middle), and a contour plot of streamwise vorticity (on the right hand side). The cross-plane survey sector is generally of sufficient size to capture the core of the resultant tip vortex. The radial axis of each plot represents distance from the wall, R-r, where R = 10.21 cms was the pipe radius. The circumferential axis represents angular position in degrees. In the interest of saving space in the figures, only the plots of secondary velocity have the survey limits in (r, θ) marked.

The vortex descriptors originate from the secondary velocity data acquired in the cross-plane. The secondary velocity data is first converted to streamwise vorticity data following the relation:

$$\omega_z = \frac{\partial v_\theta}{\partial r} + \frac{v_\theta}{r} - \frac{1}{r}\frac{\partial v_r}{\partial \theta} \qquad (3)$$

where (v_r, v_θ) are the secondary components of velocity in the radial and circumferential coordinates, respectively. Finite difference formulas are used to represent the spatial derivatives in Equation (3). In the plots of streamwise vorticity, contour lines surrounding unshaded regions represent negative values of vorticity, lines surrounding shaded regions represent positive values of vorticity. The contour increment for lines not labeled is ± 3000 sec⁻¹. ω_{max} is located at some grid point having coordinates (r_c, θ_c). The vortex circulation Γ was calculated by first isolating the region of core vorticity in the data field. This was done by plotting the "bounding value" contour of core vorticity $\omega_{zb} = 0.01\omega_{max}$, as is done in each plot of streamwise vorticity given in Figures 11-22. The circulation was then calculated according to the relation:

$$\Gamma = \iint_{\substack{core\ area \\ inside \\ bounding \\ contour}} \omega_z\, d(area) \qquad (4)$$

where ω_z is the streamwise vorticity at each elemental cross-plane area within the ω_{zb} contour. In all cases considered here, the core has a well-defined circular shape, and so Γ is easily determined. Uncertainty estimates for all listed descriptors are given in Tables 3-6. These are derived by combining the uncertainties in measured velocities and probe placement in accordance with the procedure outlined by Moffat.[19]

Isolated Vortices

Figures 11 through 19 illustrate the flow fields in the vicinity of a tip vortex shed from a single airfoil mounted in isolation. In all cases the vortex shed is a clockwise vortex. Figure 11 illustrates the effect of increasing the airfoil angle-of-attack, Figure 12 illustrates the effect of increasing the pipe core Mach number, and Figures 13 through 19 illustrate the effect of increasing the airfoil span (or alternatively, the airfoil aspect ratio 8h/πc) for each of six different airfoil chord-lengths.

Of particular interest are the contour plots of primary velocity ratio v_z/v_{zc}. These plots illustrate the vortex-airfoil wake-boundary layer interaction as well as some unexpected features of the tip vortex core. For the smaller chord-lengths of 0.85, 1.36, and 2.03 cms, the core appears as a small circular wake region with no other discernible structure. This holds true over the entire range of aspect ratio examined, $0.6 \le AR \le 6.0$. For chord-lengths at or greater than 2.54 cms, the core shows additional structural features.

Three distinct types of core structure are noted and occur according to airfoil aspect ratio:

1) For AR in the range $0.3 \leq AR \leq 1.2$ (refer to Figures 16a-c, 17a-c, 18a-d, and 19a-c) the core region appears as a small circular wake buried within the boundary layer. On the left side of the core, the boundary layer is thinned in the downwash of the vortex, on the right side it is thickened by the upwash. From the left side, a tongue of high-momentum fluid wraps under the core region and extends up the right side, creating a steep gradient in the axial velocity field in the upwash of the vortex.

2) For AR in the range $1.2 \leq AR \leq 2.5$ (refer to Figures 16d-e, 17d-f, 18e-f, and 19d-h) the vortex interaction with the boundary layer is considerably less. A portion of the upper boundary layer fluid has been convected up along the right hand side of the vortex. Structure in the core is apparent (refer to Figure 19g and 19h in particular). Within the circular confines of the core boundary, a crescent-shaped wake region surrounds a small circular region of jetting flow.

3) For AR greater than about 2.5 (refer to Figures 16f-i, 17g, and 18g) the core region is a strong circular wake with no other apparent structure. Extending below the core is the remainder of the airfoil wake.

Co-Rotating Pairs

Table 4 and Figures 20a-j present the results for co-rotating vortices shed from a pair of airfoil vortex generators of identical geometry. The spacing between airfoils (the distance s measured between the centerlines of the airfoil profiles) is nondimensionalized with the airfoil chord-length c (see Table 4). Since a co-rotating pair of vortices represents an *asymmetric* secondary flow pattern, both vortices were captured in the experiment. For the smaller spacing ratio of s/c = 0.67, the left hand and right hand vortices were captured together or plotted together (Figures 20a-e). For s/c = 1.34, the left hand and right hand vortices are plotted separately (Figures 20g-j). When compared to vortices shed from airfoils mounted in isolation, co-rotating vortices produced from pairs of airfoils of identical geometry are seen to have smaller values of circulation and peak vorticity. The measured discrepancy is between about 10 and 20%.

Counter-Rotating Up and Down Pairs

Table 5, Table 6, Figures 21a-i, and Figures 22a-i present the results for the two types of counter-rotating vortices shed from a pair of airfoils differing only in the sign (plus or minus) of α. Counter-rotating vortices represent a symmetric secondary flow pattern and so (generally speaking) only one vortex of the pair was captured in the experiment. The exceptions are at the smaller value of s/c, where some or all of the neighboring vortex was captured.

When compared to vortices shed from airfoils mounted in isolation, counter-rotating up and down vortices are seen to have enhanced values of circulation and peak vorticity (with discrepancies in the range of about 10 to 25%).

Analysis and Modeling

A portion of the results listed in Table 3 are plotted in Figures 23 to 31. The dependence of Γ and ω_{max} on α (keeping M, h/δ, and AR constant) is given in Figure 23. Both Γ (left hand plot) and ω_{max} (right hand plot) increase in approximate linear fashion with increasing α. The fall-off in ω_{max} at large α is likely due to a flow separation on the airfoil for angles greater than about 16 degrees. The dependence of Γ and ω_{max} on M (keeping α, h/δ, and AR constant) is given in Figure 25. Again, the overall character of this dependence is a linear increase in the descriptors with pipe core velocity. The dependence of Γ and ω_{max} on AR (keeping α, M, and h/δ constant) is given in Figures 25, 27, 29, and 31. Here we see Γ fall off in monotonic fashion with increasing aspect ratio. The behavior for ω_{max} is distinctly different, however. The peak vorticity first climbs to a peak and then falls off with increasing aspect ratio. The dependence of Γ and ω_{max} on h/δ (keeping α, M, and AR constant) is illustrated in Figures 26, 28, and 30. As expected, both Γ and ω_{max} increase with increasing h/δ. Peak vorticity, however, tails off at higher h/δ (Figure 30) while Γ apparently does not. Also plotted on each of Figures 23-31 are the results of analytical modeling equations developed briefly below.

Circulation

The dependence of vortex circulation on vortex generator geometry and impinging flow conditions can be approximated with an expression developed by Prandtl.[20] For a finite span wing of elliptical planform and symmetric cross-section, the circulation developed about the wing in the plane containing the wing cross-sectional profile is:

$$\Gamma = \frac{\pi \, v_{sc} \, \alpha \, c}{1 + \dfrac{2}{AR}} \qquad (5)$$

where AR = 8h/(πc). It should be noted here that, although this definition of AR applies to wings of elliptical planform, it is also used in this study to represent the AR of the rectangular planform airfoil. If we now assume that the circulation developed about the wing cross-section is turned into the stream, Equation (5) forms the basis for an expression approximating the circulation of the shed tip vortex:

$$\Gamma = \frac{k1 \, \alpha \, v_{sc} \, c}{1 + \dfrac{k2}{AR}} \tanh\left[k3 \left(\frac{h}{\delta} \right)^{k4} \right] \qquad (6)$$

where k1 and k2 replace the constants "π" and "2" in Equation (5), and the hyperbolic tangent function is used to represent the retarding influence of the boundary layer. The constants k1 through k4 are determined using a least-squares regression with the data plotted in Figures 23-31. The values are determined to be:

$$k1 = 1.61,$$
$$k2 = 0.48,$$
$$k3 = 1.41,$$
$$k4 = 1.00.$$

As the figures indicate, Equation (6) provides an excellent correlation for the initial circulation behavior of the tip vortices.

Peak Vorticity

In remarkably accurate fashion, Prandtl's inviscid analysis provides us with an estimate of shed vortex circulation. Γ can be viewed as the integration or summation of the streamwise vorticity field. Peak vorticity, on the other hand, is an element of the streamwise vorticity field's distribution or "structure". Nothing of this structure can be discerned from the inviscid analysis. In fact, it may be noted that the inviscid model of a vortex has an infinite (and therefore unphysical) value of peak vorticity at the core central location (and a zero value everywhere else). Thus, to begin our analysis for ω_{max}, we discard the inviscid model and consider, instead, a viscous vortex. Perhaps the simplest model of a viscous vortex is the Lamb vortex. The Lamb vortex is obtained through classical solution techniques of the Navier-Stokes equations simplified to represent two-dimensional axisymmetric flow.[21] Simply stated; a Lamb vortex is a time dependent axisymmetric viscous flow that starts as a potential vortex. The velocity at the origin (r = 0, center of the vortex) is forced to zero at time t = 0. The resulting solution describes the subsequent decay in terms of angular velocity v_θ. In radial coordinates this is:

$$v_\theta = \frac{\Gamma}{2\pi r} \left(1.0 - \exp\left\{ \frac{-r^2}{4\nu t} \right\} \right) \qquad (7)$$

where Γ here is the limiting value of vortex circulation (as $r \to \infty$), ν is the coefficient characterizing the viscous diffusion of the flow, and r is the radial coordinate, measured from the center of the vortex (crossplane origin). As before, let z represent the streamwise or axial coordinate. Replace t with the streamwise convective displacement $t \approx z/v_{zc}$ (with the origin of the streamwise coordinate coinciding with t = 0) and differentiate $v_\theta(r,z)$ to obtain the streamwise vorticity field:

$$\omega_z = \frac{v_{zc}\Gamma}{4\pi\nu z} \exp\left\{ \frac{-v_{zc} r^2}{4\nu z} \right\}. \qquad (8)$$

The peak vorticity is thus: $\omega_{max} = v_{zc}\Gamma/(4\pi\nu z)$. Substitute for ν and t in Equation (7) to find:

$$v_\theta = \frac{\Gamma}{2\pi r} \left(1.0 - \exp\left\{ \frac{-\pi\omega_{max} r^2}{\Gamma} \right\} \right) \qquad (9)$$

or, in other words, the Lamb vortex in terms of circulation and peak vorticity.[14] This form (see also Equation 1) aids the modeling process, since (as we have seen from the previous section) it requires information (or data) about the vortex in the vicinity of the core only, where the circulation and peak vorticity are entirely contained. If, for example, we chose to write Equation (9) in terms of the conserved properties of vortex crossplane angular momentum or kinetic energy, a researcher would be required to obtain information over the entire flow field.

To proceed with the analysis for ω_{max}, we make the following two assumptions:

1) At the "initial" streamwise location (in this study we assume the z = 1 chord-length position) vortex structure can be accurately represented by the Lamb vortex model. As indicated earlier in the "Introduction and Background" section, many previous studies exist to support this assumption.

2) The conserved property of vortex angular momentum can be related to a pressure force moment formulated near the airfoil tip.

By integrating a suitable version of the Lamb vortex to obtain an expression for angular momentum, and through the use of Prandtl's equation for Γ (Equation 6) we will isolate ω_{max} in terms of vortex generator geometry and impinging flow conditions. Lets start first by developing the conservation relationship.

Estimating Tip Vortex Angular Momentum Production

The rate of vortex angular momentum production is equated to a moment summation taken at the airfoil tip. Reference 22 is a very good experimental description of the vortex roll-up phenomena in the vicinity of the airfoil tip. In Reference 22, the airfoil is a large scale half-wing model (similar to the models tested in this report) with a NACA-0012 sectional profile. Let H be the angular momentum of the shed vortex, CF a characteristic force tending to rotate the fluid at the wing tip, and CMA a characteristic moment arm through which the fluid is rotated. Then:

$$\sum (moments\ at\ the\ tip) = CF \times CMA =$$
$$\frac{\partial H}{\partial t} \approx v_{zc} \frac{H}{dz}. \qquad (10)$$

CF is related to the lift force on the airfoil and is estimated by integrating the 2D inviscid pressure distribution:[23]

$$\Delta C_p = 4.0 \; (\sin \alpha) \; \sqrt{\frac{c}{z} - 1} \qquad (11)$$

over the surface of the airfoil:

$$CF = 2.0 \; \rho v_{\infty}^2 \; \alpha c \int_{y_{ll}}^{h} \int_{0}^{c} \sqrt{\frac{c}{z} - 1} \; \frac{dz}{c} \; dy \qquad (12)$$

where y_{ll} represents the lower limit on the span component of integration, and ρ represents the fluid density. By setting $y_{ll} = 0$ we confine our analysis to "small" aspect ratios. This follows because, as the aspect ratio of the airfoil increases and the span grows out of proportion to the chord, the lift forces generated near the root (or wall location) have less of an influence at the tip. Thus, at larger aspect ratios, Equation (9) with $y_{ll} = 0$ tends to overestimate CF.

CMA is taken to be the radius of the shed vortex. We approximate this by an expression for r_{max}, the radial location at which v_θ (from Equation 9) is maximum:

$$CMA \approx r_{max} = \sqrt{\frac{\Gamma}{2 \pi \omega_{max}}}. \qquad (13)$$

Equation (13) for CMA describes what is also known as the "Rankine" core radius of a viscous vortex.

Integrate Equation (12), substitute this expression with Equation (13) into Equation (10) to obtain:

$$\frac{\sum (moments \;\; at \;\; tip)}{\rho v_{\infty}} = \frac{H}{\rho \, dz} \approx \pi \, \alpha \, c \, h \, v_{\infty} \sqrt{\frac{\Gamma}{2 \pi \omega_{max}}}. \qquad (14)$$

We now turn our attention to integrating the Lamb vortex model for angular momentum H.

Angular Momentum of the Constrained Lamb Vortex

The angular momentum in a region of the polar crossplane bounded by η: $0 \le \eta \le r$ and θ: $0 \le \theta \le 2\pi$ is evaluated with the expression:

$$\frac{H}{\rho \;\; dz} = \int_{0}^{2\pi} \int_{0}^{r} (\vec{r} \times \vec{v}) \;\; 2\pi \eta \;\; d\eta \;\; d\theta \qquad (15)$$

where $\vec{v}$ represents the secondary or crossplane velocity vector. Applying Equation (15) to Equation (9) provides the angular momentum profile of the Lamb vortex:

$$\frac{H}{\rho \, dz} = \Gamma \left[\frac{r^2}{2} - \frac{\Gamma}{2\pi \omega_{max}} \left(1 - \exp \left\{ \frac{-\pi \omega_{max} r^2}{\Gamma} \right\} \right) \right]. \qquad (16)$$

It can be seen from this expression that the angular momentum (per unit axial dimension) is unbounded in r, or in other words, $H(\rho \;\; dz) \to \infty$ as $r \to \infty$. Thus, before we can use the Lamb vortex in this analysis, a meaningful way to constrain it (in r) must be found. One approach[24] is to define a model discontinuous in v_θ. Figure 32 diagrams this construction. Figure 32 is a plot of v_θ versus r as defined by Equation (9) for indicated values of circulation and peak vorticity. Define a velocity ratio ς:

$$\varsigma = \frac{v_\theta}{v_{\theta \, max}} \qquad (17)$$

where $v_{\theta max}$ is the maximum angular velocity of the Lamb vortex over the range r: $0 \le r < \infty$. As Figure 32 indicates, this velocity ratio is realized at two radial locations on the Lamb vortex profile, r1 and r2. Choose r2 to be the outer boundary of this discontinuous vortex model, referred to here as the "constrained Lamb vortex". Note, from Figure 32, that by choosing r2 and $\varsigma \ll 1.0$, all of the viscous core and a good portion of the inviscid outer region of the Lamb vortex are retained. Now r2 can be approximated:

$$r2 \approx \frac{1}{\varsigma \left(1 - e^{-1/2} \right)} \sqrt{\frac{\Gamma}{2 \pi \omega_{max}}}. \qquad (18)$$

Apply Equation (15) within this boundary to find:

$$\frac{H}{\rho \, dz} = \frac{\Gamma^2}{2 \pi \omega_{max}} \left[\beta - 1 + e^{-\beta} \right] \qquad (19)$$

where:

$$\beta = \frac{1}{2 \varsigma^2 \left(1 - e^{-1/2} \right)^2}. \qquad (20)$$

Equation (19) is simplified to:

$$\frac{H}{\rho \, dz} \approx \frac{\Gamma^2 (\beta - 1)}{2 \pi \omega_{max}} \qquad (21)$$

Note that the angular momentum of the constrained Lamb vortex is proportional to Γ^2/ω_{max}. Other vortex models have been examined (both continuous and discontinuous in v_θ) to determine the angular momentum relationships and these are also found to be proportional to Γ^2/ω_{max}.[24]

Returning now to Equation (14):

$$\frac{H}{\rho \, dz} = \pi \, \alpha \, c \, h \, v_{\infty} \sqrt{\frac{\Gamma}{2 \pi \omega_{max}}}$$

we replace the left hand side with Equation (21) and solve for ω_{max} to find:

$$\omega_{max} = \frac{\Gamma^3 (\beta - 1)^2}{2\pi^3 \alpha^2 c^2 h^2 v_{zc}^2}.$$ (22)

The constant ζ from Equation (17) was determined by a least squares regression from the plotted peak vorticity data on Figures 23 through 31. The value was determined to be $\zeta = 0.29$. The peak vorticity plots (right hand side of Figures 23 through 31) illustrate the correlation of Equation (22) with the given value of ζ. Overall, a very good qualitative agreement with the data is obtained.

Summary

An extensive parametric study of vortices shed from airfoil vortex generators has been conducted to determine the dependence of initial vortex circulation Γ and peak vorticity ω_{max} on airfoil angle-of-attack α, chordlength c, span h, impinging external Mach number M, and boundary layer thickness δ. In addition, the influence of airfoil-to-airfoil spacing on Γ and ω_{max} has been examined for pairs of airfoils producing co-rotating and counter-rotating vortices.

The vortex generators were symmetric airfoils having NACA-0012 cross-sections. These airfoils were mounted either in isolation or in pairs on the surface of a straight pipe. The turbulent boundary layer thickness to pipe radius ratio was $\delta/R \approx 0.17$. The circulation and peak vorticity data were derived from cross-plane velocity measurements acquired with a seven-hole probe at one chord length downstream of the airfoil trailing edge location.

Γ is observed to be proportional to M, α, and h/δ. With these parameters held constant, Γ is observed to fall off in monotonic fashion with increasing airfoil aspect ratio AR = 8h/πc. ω_{max} is also observed to be proportional to M, α, and h/δ. Unlike Γ, however, ω_{max} is observed to increase with increasing aspect ratio, reaching a peak value at AR $\approx$ 2.0 before falling off and rising again at higher values of AR. Co-rotating vortices shed from closely-spaced pairs of airfoils have values of Γ and ω_{max} under those values found for vortices shed from isolated airfoils of the same geometry. Conversely, counter-rotating vortices show enhanced values of Γ and ω_{max} when compared to values obtained in isolation.

Γ may be accurately modeled with an expression based on Prandtl's relationship between finite airfoil circulation and airfoil geometry. A correlation for ω_{max} has been derived from a conservation relationship equating the moment at the airfoil tip to the rate of angular momentum production of the shed vortex, modeled as a Lamb (viscous) vortex. This technique provides excellent qualitative agreement to the observed behavior of ω_{max} for low aspect ratio airfoils typically used as vortex generators.

References

[1]Reichert, B.A. and Wendt, B.J., "Improving Diffusing S-Duct Performance by Secondary Flow Control," AIAA Paper 94-0365, Jan. 1994.

[2]Foster, J., Okiishi, T.H., Wendt, B.J., and Reichert, B.A., "Study of Compressible Flow Through a Rectangular-to-Semiannular Transition Duct," NASA CR-4660, Apr. 1995.

[3]Wendt, B.J. and Dudek, J.C., "Development of Vortex Generator Use for a Transitioning High Speed Inlet," *Journal of Aircraft*, Vol. 35, No. 4, August 1998, pp. 536-543.

[4]Hamstra, J.W., Miller, D.N., Truax, P.P., Anderson, B.A., and Wendt, B.J., "Active Inlet Flow Control Technology Demonstration," 22nd International Council of Aeronautical Sciences, ICAS Paper 6112, August 2000.

[5]Wendt, B.J., "Suppression of Cavity-Driven Flow Separation in a Simulated Mixed Compression Inlet," NASA/CR—2000-210460, September 2000.

[6]Anderson, B.H. and Gibb, J., "Application of Computational Fluid Dynamics to the study of Vortex Flow Control for the Management of Inlet Distortion," AIAA Paper 92-3177, July 1992.

[7]Anderson, B.H. and Gibb, J., "Vortex Generator Installation Studies on Steady State and Dynamic Distortion," AIAA Paper 96-3279, July 1996.

[8]Anderson, B.H. and Farokhi, S., "A Study of Three Dimensional Turbulent Boundary Layer Separation and Vortex Flow Control Using the Reduced Navier-Stokes Equations," Turbulent Shear Flow Symposium Technical Report, 1991.

[9]Bender, E.E., Anderson, B.H., and Yagle, P.J., "Vortex Generator Modeling for Navier-Stokes Codes," Symposium on Flow Control of Wall Bounded and Free Shear Flow, 1996 Joint ASME/JSME Fluids Engineering Conference, San Francisco, CA, July 18-22, 1999.

[10]Wendt, B.J., Reichert, B.A., and Foster, J.D., "The Decay of Longitudinal Vortices Shed from Airfoil Vortex Generators," AIAA Paper 95-1797, June 1995.

[11]Westphal, R.V., Pauley, W.R. and Eaton, J.K., "Interaction Between a Vortex and a Turbulent Boundary Layer-Part 1: Mean Flow Evolution and Turbulence Properties," NASA TM-88361, January 1987.

[12]Wendt, B.J. and Reichert, B.A., "The Modelling of Symmetric Airfoil Vortex Generators," AIAA Paper 96-0807, June 1996.

[13]Pauley, W.R. and Eaton, J.K., "The Fluid Dynamics and Heat Transfer Effects of Streamwise Vortices Embedded in a Turbulent Boundary Layer," Stanford University Technical Report MD-51, Stanford, CA, August 1988.

[14]Wendt, B.J., Greber, I., and Hingst, W.R., "The Structure and Development of Streamwise Vortex Arrays Embedded in a Turbulent Boundary Layer," AIAA Paper 92–0551, January 1992.

[15]Wendt, B.J. and Hingst, W.R., "Flow Structure in the Wake of a Wishbone Vortex Generator," *AIAA Journal*, Vol. 32, November 1994, pp. 2234–2240.

[16]Wendt, B.J. and Reichert, B.A., "Spanwise Spacing Effects on the Initial Structure and Decay of Axial Vortices," NASA CR–198544, November 1996.

[17]Porro, A.R., Hingst, W.R., Wasserbauer, C.A., and Andrews, T.B., "The NASA Lewis Research Center Internal Fluid Mechanics Facility," NASA TM–105187, September 1991.

[18]Zilliac, G.G., "Modelling, Calibration, and Error Analysis of Seven-Hole Probes," *Experiments in Fluids*, Vol. 14, 1993, pp. 104–120.

[19]Moffat, R.J., "Contributions to the Theory of Single-Sample Uncertainty Analysis," *Transactions of the ASME*, Vol. 104, June 1982, pp. 250–258.

[20]Prandtl, L., "Applications of Modern Hydrodynamics to Aeronautics," NACA Report 116, 1921.

[21]Panton, R.L., *Incompressible Flow*, 1st Edition, John Wiley and Sons, New York, 1984. See Chapter 11.

[22]Chow, J.S., Zilliac, G.G., and Bradshaw, P., "Measurements in the Near-Field of a Turbulent Wing-Tip Vortex," AIAA Paper 93–0551, January 1993.

[23]Karamcheti, K., "*Principles of Ideal-Fluid Aerodynamics*," 1st Edition, John Wiley and Sons, New York, 1966. See Chapter 17.

[24]Wendt, B.J., "Initial Peak Vorticity Behavior for Vortices Shed from Airfoil Vortex Generators," AIAA Paper 98–0693, January 1998.

[25]Bray, T.P., "A Parametric Study of Vane and Air-jet Vortex Generators," Cranfield University Engineering Doctorate, BCC/DERA, October 1998.

vane vortex generators

Flow

throat cross-section
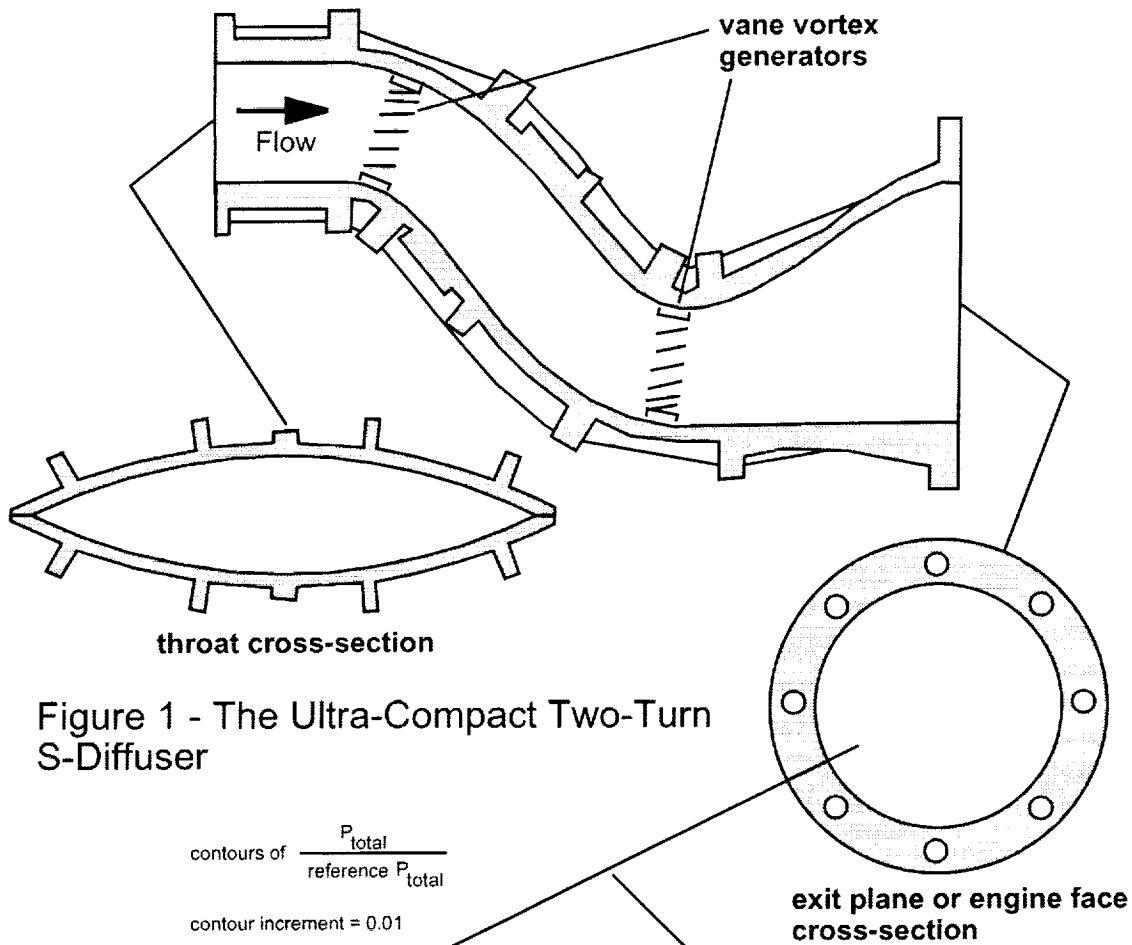
Figure 1 - The Ultra-Compact Two-Turn S-Diffuser

contours of $\dfrac{P_{total}}{\text{reference } P_{total}}$

contour increment = 0.01

exit plane or engine face cross-section

Baseline (no VGs)
Recovery = 0.910
DC60 Distortion = 0.390

Vane Span = 2 mm
Recovery = 0.957
DC60 Distortion = 0.170
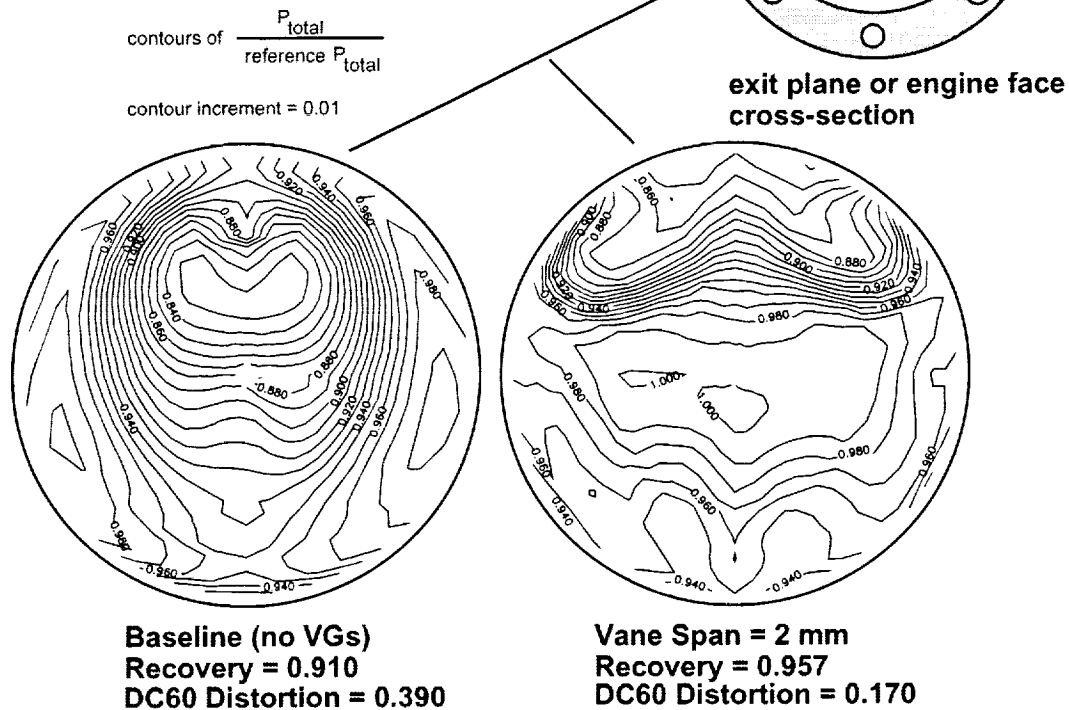
Figure 2 - Vane vortex generators dramatically change total pressure contours at the engine face for the two-turn S-diffuser.

degrees   degrees
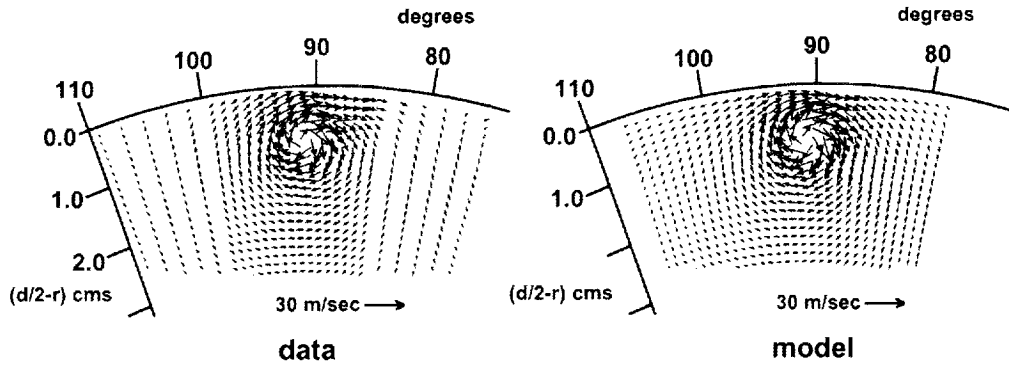
data   model

Figure 3 - A comparison of the secondary velocity field of an embedded vortex; data on the left, and a model constructed from the superposition of Lamb vortices on the right.
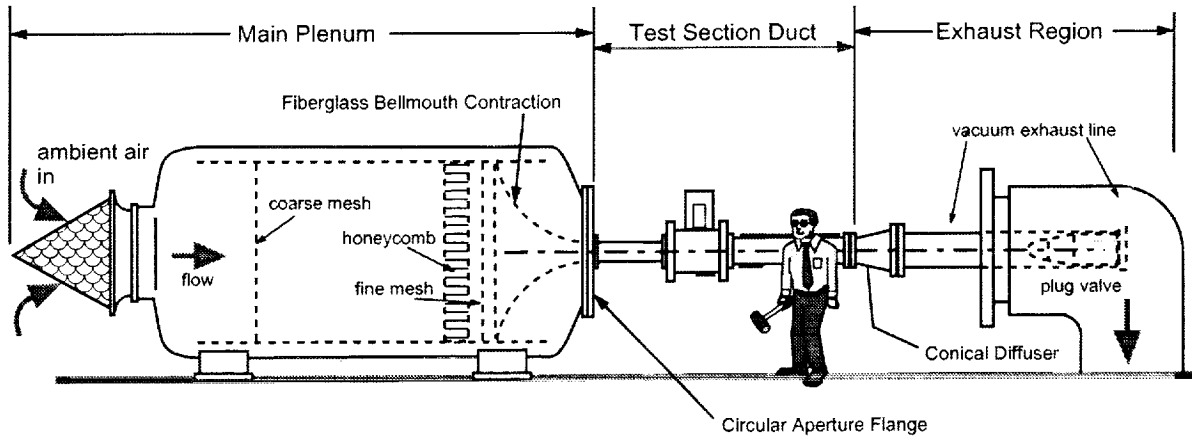
Figure 4 - The Internal Fluid Mechanics Facility of NASA Glenn
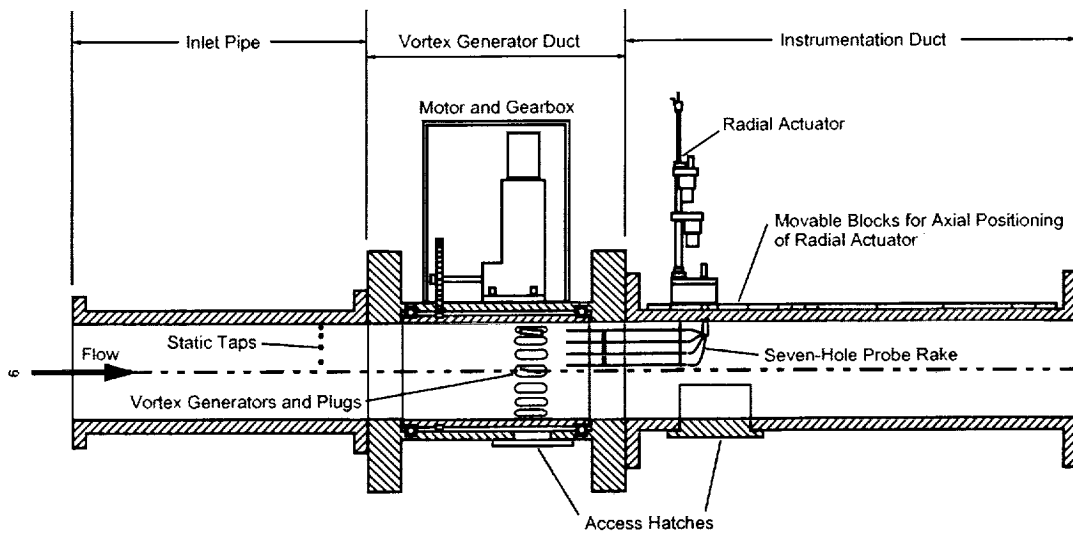
Figure 5 - A cut-away sketch of the test section duct.

h (span)

Side View   Front View

c, chord

alpha

Top View   Single Airfoil VG
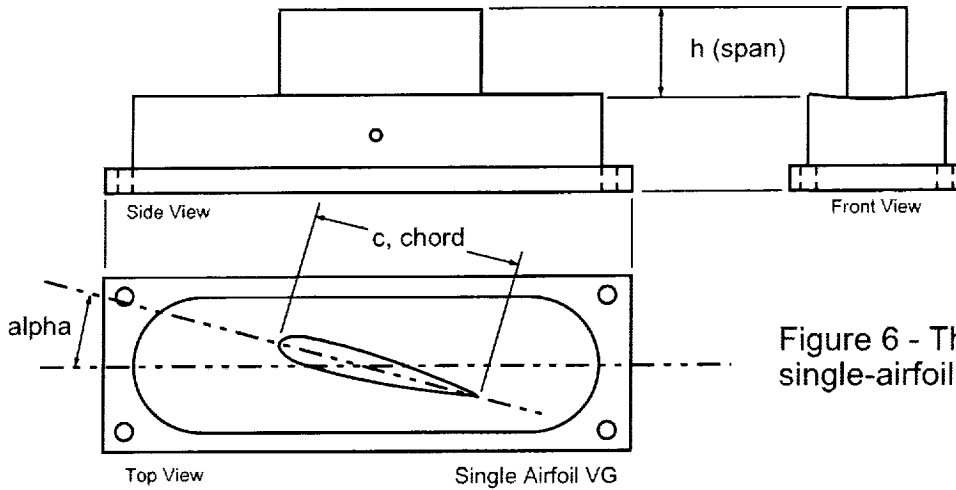
Figure 6 - The geometry of the single-airfoil vortex generator.

Table 1 - Summary of single-airfoil geometry, covering all models tested.

chord c (cms)	span h (cms)	angle-of-attack α (degs)	notes
0.85	0.21	16	
0.85	0.51	16	
0.85	1.02	16	
0.85	1.52	16	
0.85	2.03	16	
1.36	0.28	16	
1.36	0.51	16	
1.36	0.81	16	
1.36	1.02	16	
1.36	1.52	16	
1.36	1.63	16	
1.36	2.03	16	
1.36	2.54	16	
1.36	3.05	16	
1.36	3.56	16	
2.03	0.51	16	
2.03	1.02	16	
2.03	1.22	16	
2.03	1.52	16	
2.03	2.03	16	
2.03	2.44	16	
2.54	0.51	16	
2.54	0.64	16	
2.54	1.02	16	
2.54	1.52	16	
2.54	2.03	16	
2.54	2.54	16	
2.54	3.05	16	
2.54	3.56	16	
2.54	4.57	16	

chord c (cms)	span h (cms)	angle-of-attack α (degs)	notes
3.05	0.51	16	
3.05	0.76	16	
3.05	1.02	16	
3.05	1.52	16	
3.05	1.83	16	
3.05	2.03	16	
3.05	3.66	16	
3.56	0.51	16	
3.56	0.89	16	
3.56	1.02	16	
3.56	1.52	16	
3.56	2.03	16	
3.56	2.13	16	
3.56	4.27	16	
4.06	0.51	+/- 16	a, b, c
4.06	1.02	8	
4.06	1.02	12	
4.06	1.02	+/- 16	d
4.06	1.02	20	
4.06	1.52	+/- 16	a, b, c
4.06	2.03	16	
4.06	2.44	16	
4.06	2.54	+/- 16	a, b, c
4.06	3.05	16	
4.06	3.56	16	

Notes:
a) used in co-rotating pairs
b) used in counter-rotating up pairs
c) used in counter-rotating down pairs
d) used in full counter-rotating arrays.
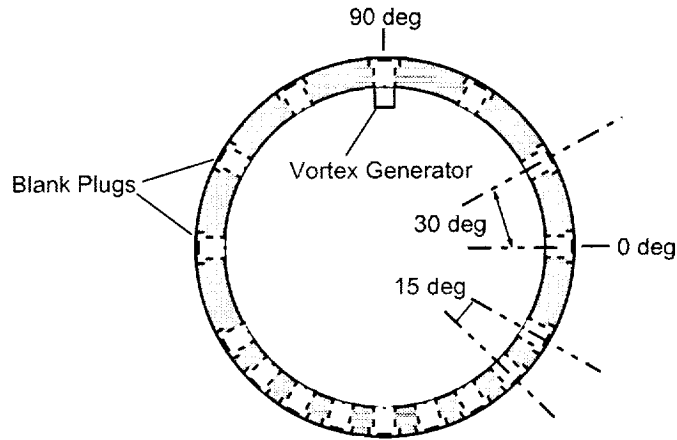
Figure 7 - The r-theta crossplane looking upstream into the vg duct.
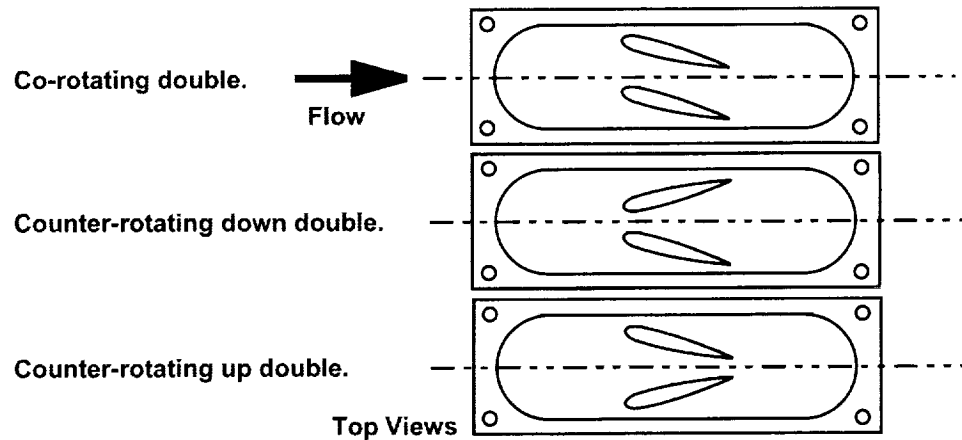
Figure 8 - The geometry of the double-airfoil vortex generators (c = 1.36 cms).

Table 2 - Summary of double-airfoil geometry, covering all models tested			
chord c (cms)	span h (cms)	α (deg)	double-airfoil type
1.36	1.02	16	co-rotating double airfoil
1.36	2.03	16	co-rotating double airfoil
1.36	0.51	+/- 16	counter-rotating down double airfoil
1.36	1.02	+/- 16	counter-rotating down double airfoil
1.36	2.03	+/- 16	counter-rotating down double airfoil
1.36	0.51	+/- 16	counter-rotating up double airfoil
1.36	1.02	+/- 16	counter-rotating up double airfoil
1.36	2.03	+/- 16	counter-rotating up double airfoil

Figure 9 - The single seven-hole probe shown in a cut-away view of the test section. The tip could be adjusted in the axial component to acquire data one chord-length downstream of the vortex generator airfoil.
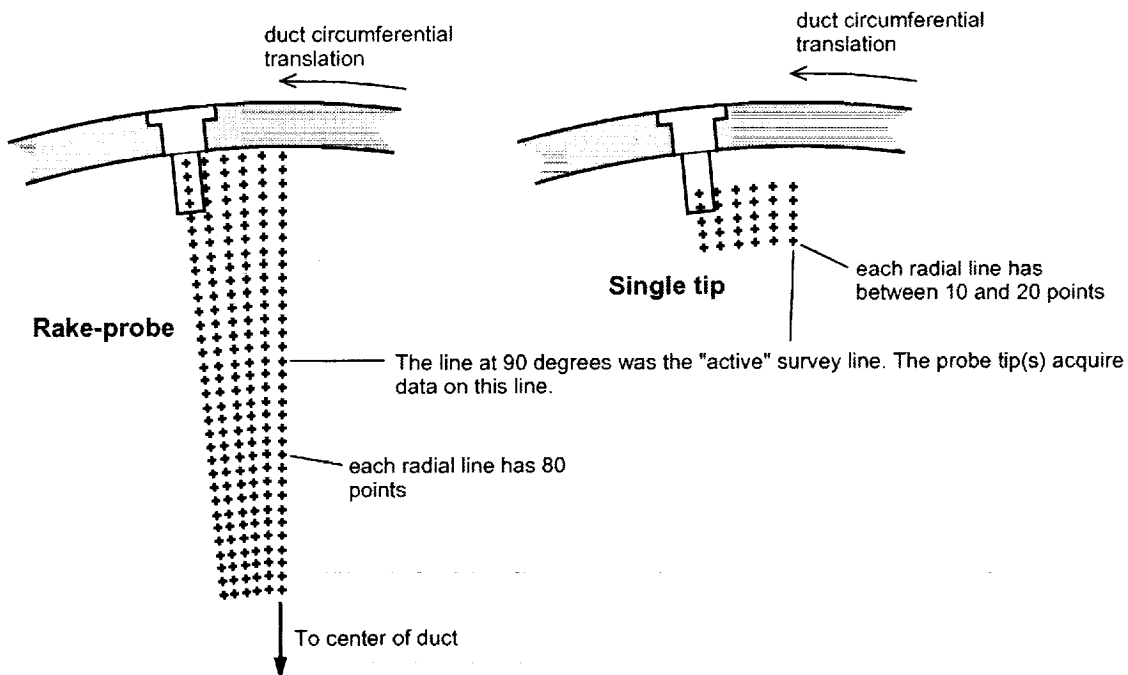
Figure 10 - The survey grids used by the seven-hole probe rake and single tip.

Table 3

Results for Isolated Airfoils, and Airfoils Tested in Full Counter-Rotating Arrays.

α deg	c cms	h cms	AR	h/δ	v_{zc} m/sec	Mach	Γ m^2/sec	ω_{max} 1/sec	See Fig.
8	4.06	1.02	0.64	0.57	85	0.25	-0.291	-18193	11a
12	4.06	1.02	0.64	0.57	85	0.25	-0.471	-24346	11b
16	4.06	1.02	0.64	0.57	85	0.25	-0.643	-33189	11c
20	4.06	1.02	0.64	0.57	85	0.25	-0.940	-34055	11d
16 *	4.06	1.02	0.64	0.57	85	0.25	-0.722	-35714	12a
16 *	4.06	1.02	0.64	0.62	129	0.40	-1.149	-56831	12b
16 *	4.06	1.02	0.64	0.65	187	0.60	-1.724	-84000	12c
16	0.85	0.21	0.64	0.12	85	0.25	-0.156	-20297	13a
16	0.85	0.51	1.53	0.29	85	0.25	-0.240	-22340	13b
16	0.85	1.02	3.06	0.57	85	0.25	-0.253	-30881	13c
16	0.85	1.52	4.58	0.86	85	0.25	-0.297	-33368	13d
16	0.85	2.03	6.11	1.14	85	0.25	-0.307	-38301	13e
16	1.36	0.28	0.64	0.19	85	0.25	-0.223	-29194	14a
16	1.36	0.51	0.96	0.29	85	0.25	-0.342	-23734	14b
16	1.36	0.81	1.53	0.46	85	0.25	-0.315	-42509	14c
16	1.36	1.02	1.91	0.57	85	0.25	-0.315	-35415	14d
16	1.36	1.52	2.86	0.86	85	0.25	-0.429	-37397	14e
16	1.36	1.63	3.06	0.91	85	0.25	-0.419	-52295	14f
16	1.36	2.03	3.82	1.14	85	0.25	-0.485	-50676	14g
16	1.36	2.54	4.78	1.43	85	0.25	-0.428	-44093	14h
16	1.36	3.05	5.73	1.71	85	0.25	-0.476	-60375	14i
16	1.36	3.56	6.68	2.00	85	0.25	-0.446	-63832	14j
16	2.03	0.51	0.64	0.29	85	0.25	-0.322	-27772	15a
16	2.03	1.02	1.27	0.57	85	0.25	-0.435	-43956	15b
16	2.03	1.22	1.53	0.69	85	0.25	-0.493	-52181	15c
16	2.03	1.52	1.91	0.86	85	0.25	-0.552	-57278	15d
16	2.03	2.03	2.55	1.14	85	0.25	-0.596	-56235	15e
16	2.03	2.44	3.06	1.37	85	0.25	-0.667	-44619	15f
16	2.54	0.51	0.51	0.29	85	0.25	-0.450	-22914	16a
16	2.54	0.64	0.64	0.36	85	0.25	-0.421	-31387	16b
16	2.54	1.02	1.02	0.57	85	0.25	-0.525	-43913	16c
16	2.54	1.52	1.53	0.86	85	0.25	-0.626	-57104	16d
16	2.54	2.03	2.04	1.14	85	0.25	-0.719	-73333	16e
16	2.54	2.54	2.55	1.43	85	0.25	-0.781	-58750	16f
16	2.54	3.05	3.06	1.71	85	0.25	-0.825	-42748	16g
16	2.54	3.56	3.56	2.00	85	0.25	-0.862	-46882	16h
16	2.54	4.57	4.58	2.57	85	0.25	-0.866	-70289	16i
16	3.05	0.51	0.42	0.29	85	0.25	-0.399	-23345	17a
16	3.05	0.76	0.64	0.43	85	0.25	-0.530	-30924	17b
16	3.05	1.02	0.85	0.57	85	0.25	-0.591	-40099	17c
16	3.05	1.52	1.27	0.86	85	0.25	-0.704	-53251	17d
16	3.05	1.83	1.53	1.03	85	0.25	-0.776	-59852	17e
16	3.05	2.03	1.70	1.14	85	0.25	-0.817	-58695	17f
16	3.05	3.66	3.06	2.06	85	0.25	-0.985	-35505	17g

* Data from full counter-rotating airfoil arrays.   +/- 5%   +/- 7%

Table 3 - Continued
Results for Isolated Airfoils, and Airfoils Tested in Full Counter-Rotating Arrays.

α deg	c cms	h cms	AR	h/δ	v_{zc} m/sec	Mach	Γ m²/sec	ω_{max} 1/sec	See Fig.
16	3.56	0.51	0.36	0.29	85	0.25	-0.451	-21114	18a
16	3.56	0.89	0.64	0.50	85	0.25	-0.662	-36897	18b
16	3.56	1.02	0.73	0.57	85	0.25	-0.648	-40085	18c
16	3.56	1.52	1.09	0.86	85	0.25	-0.780	-54079	18d
16	3.56	2.03	1.46	1.14	85	0.25	-0.944	-59439	18e
16	3.56	2.13	1.53	1.20	85	0.25	-0.941	-67331	18f
16	3.56	4.27	3.06	2.40	85	0.25	-1.170	-45710	18g
16	4.06	0.51	0.32	0.29	85	0.25	-0.429	-19956	19a
16	4.06	1.02	0.64	0.57	85	0.25	-0.713	-39161	19b
16	4.06	1.52	0.96	0.86	85	0.25	-0.824	-50476	19c
16	4.06	2.03	1.27	1.14	85	0.25	-0.961	-60834	19d
16	4.06	2.44	1.53	1.37	85	0.25	-1.044	-63493	19e
16	4.06	2.54	1.59	1.43	85	0.25	-1.045	-66113	19f
16	4.06	3.05	1.91	1.71	85	0.25	-1.210	-66124	19g
16	4.06	3.56	2.23	2.00	85	0.25	-1.243	-69638	19h

+/- 5%   +/- 7%

Table 4
Results for Co-Rotating Pairs

α deg	c cms	h cms	AR	h/δ	Left Hand or Right Hand	s/c	v_{zc} m/sec	Mach	Γ m²/sec	ω_{max} 1/sec	See Fig.
16	1.36	1.02	1.91	0.57	LH	0.67	85	0.25	-0.284	-35786	20a
16	1.36	1.02	1.91	0.57	RH	0.67	85	0.25	-0.305	-32902	20a
16	1.36	2.03	3.82	1.14	LH	0.67	85	0.25	-0.398	-35994	20b
16	1.36	2.03	3.82	1.14	RH	0.67	85	0.25	-0.437	-55409	20b
16	4.06	0.51	0.32	0.29	LH	0.67	85	0.25	-0.397	-17349	20c
16	4.06	0.51	0.32	0.29	RH	0.67	85	0.25	-0.462	-18203	20c
16	4.06	1.52	0.95	0.86	LH	0.67	85	0.25	-0.667	-40248	20d
16	4.06	1.52	0.95	0.86	RH	0.67	85	0.25	-0.742	-42782	20d
16	4.06	2.54	1.59	1.43	LH	0.67	85	0.25	-0.879	-48733	20e
16	4.06	2.54	1.59	1.43	RH	0.67	85	0.25	-0.954	-55171	20e
16	4.06	0.51	0.32	0.29	LH	1.34	85	0.25	-0.480	-19411	20g
16	4.06	0.51	0.32	0.29	RH	1.34	85	0.25	-0.482	-19853	20f
16	4.06	1.52	0.95	0.86	LH	1.34	85	0.25	-0.794	-49131	20i
16	4.06	1.52	0.95	0.86	RH	1.34	85	0.25	-0.794	-43568	20h
16	4.06	2.54	1.59	1.43	LH	1.34	85	0.25	-1.021	-62701	20k
16	4.06	2.54	1.59	1.43	RH	1.34	85	0.25	-1.012	-56314	20j

+/- 5%   +/- 7%

Table 5
Results for Counter-Rotating Up Pairs

α deg	c cms	h cms	AR	h/δ	Left Hand or Right Hand	s/c	v_{zc} m/sec	Mach	Γ m²/sec	ω_{max} 1/sec	See Fig.
16	1.36	0.51	0.95	0.29	LH	0.67	85	0.25	-0.269	-28385	21a
16	1.36	0.51	0.95	0.29	RH	0.67	85	0.25	+0.275	+28276	21a
16	1.36	1.02	1.91	0.57	LH	0.67	85	0.25	-0.402	-36723	21b
16	1.36	1.02	1.91	0.57	RH	0.67	85	0.25	+0.403	+40026	21b
16	1.36	2.03	3.82	1.14	LH	0.67	85	0.25	-0.567	-39639	21c
16	1.36	2.03	3.82	1.14	RH	0.67	85	0.25	+0.545	+45039	21c
16	4.06	0.51	0.32	0.29	LH	0.67	85	0.25	-0.580	-21634	21d
16	4.06	0.51	0.32	0.29	RH	0.67	85	0.25	>+0.422	+19828	21d
16	4.06	1.52	0.95	0.86	LH	0.67	85	0.25	-1.120	-56758	21e
16	4.06	2.54	1.59	1.43	LH	0.67	85	0.25	-1.340	-66147	21f
16	4.06	0.51	0.32	0.29	LH	1.34	85	0.25	-0.499	-18690	21g
16	4.06	1.52	0.95	0.86	LH	1.34	85	0.25	-0.916	-49315	21h
16	4.06	2.54	1.59	1.43	LH	1.34	85	0.25	-1.201	-69724	21i

+/- 5%   +/- 7%

Table 6
Results for Counter-Rotating Down Pairs

α deg	c cms	h cms	AR	h/δ	Left Hand or Right Hand	s/c	v_{zc} m/sec	Mach	Γ m²/sec	ω_{max} 1/sec	See Fig.
16	1.36	0.51	0.95	0.29	LH	0.67	85	0.25	+0.280	+29840	22a
16	1.36	0.51	0.95	0.29	RH	0.67	85	0.25	-0.290	-31244	22a
16	1.36	1.02	1.91	0.57	LH	0.67	85	0.25	+0.401	+30432	22b
16	1.36	1.02	1.91	0.57	RH	0.67	85	0.25	-0.371	-45129	22b
16	1.36	2.03	3.82	1.14	RH	0.67	85	0.25	-0.494	-29692	22c
16	4.06	0.51	0.32	0.29	RH	0.67	85	0.25	-0.516	-21336	22d
16	4.06	1.52	0.95	0.86	RH	0.67	85	0.25	-1.064	-56439	22e
16	4.06	2.54	1.59	1.43	RH	0.67	85	0.25	-1.326	-68872	22f
16	4.06	0.51	0.32	0.29	RH	1.34	85	0.25	-0.465	-19842	22g
16	4.06	1.52	0.95	0.86	RH	1.34	85	0.25	-0.917	-53157	22h
16	4.06	2.54	1.59	1.43	RH	1.34	85	0.25	-1.215	-67317	22i

+/- 5%   +/- 7%

a) alpha = 8 degrees, circulation = -0.291 m2/sec, peak vorticity = -18193 sec-1

b) alpha = 12 degrees, circulation = -0.471 m2/sec, peak vorticity = -24346 sec-1

c) alpha = 16 degrees, circulation = -0.643 m2/sec, peak vorticity = -33189 sec-1

d) alpha = 20 degrees, circulation = -0.940 m2/sec, peak vorticity = -34055 sec-1
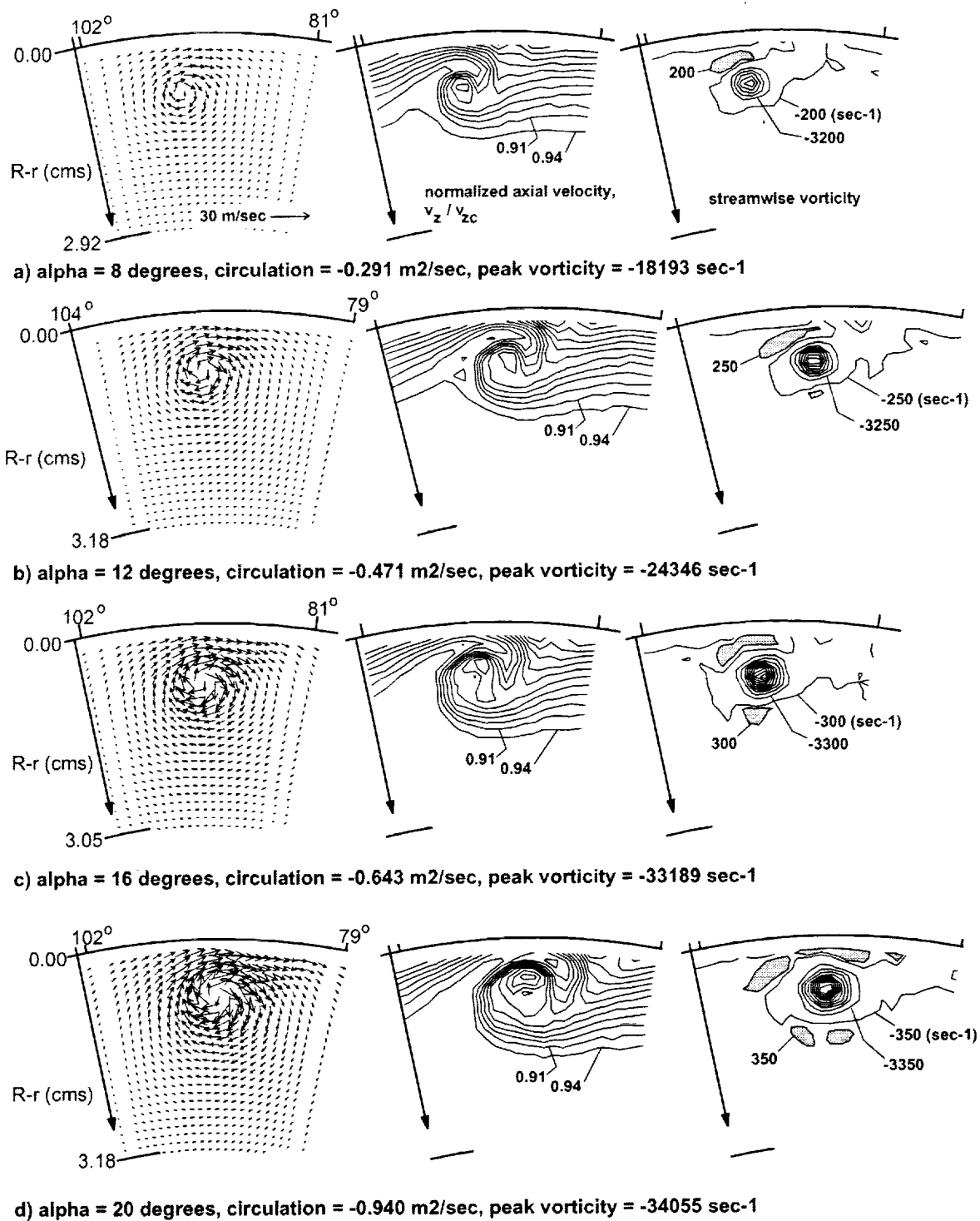
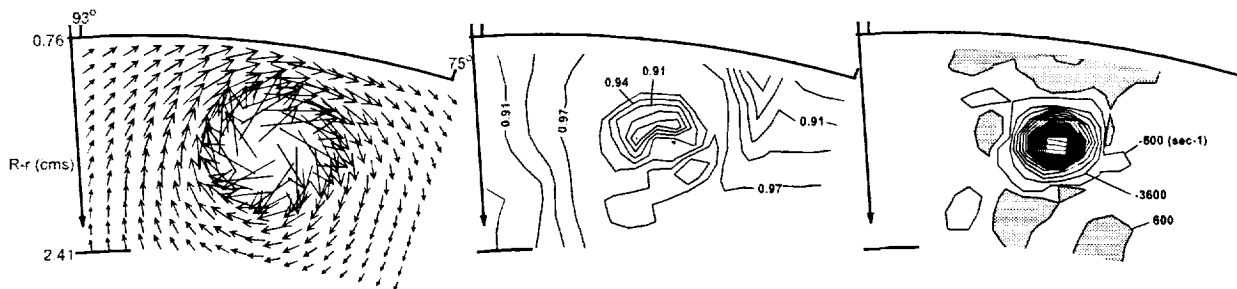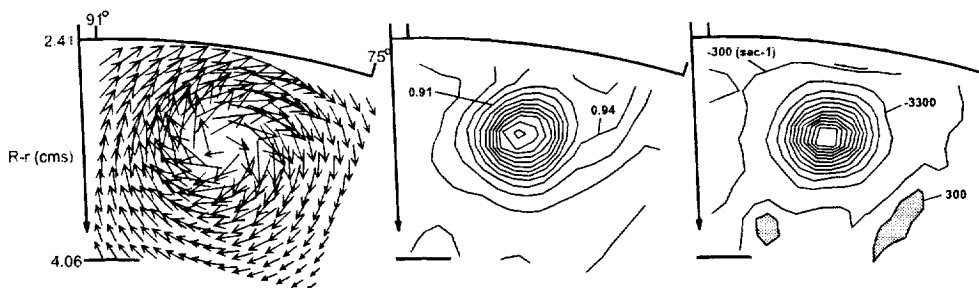Figure 11 - Velocity and streamwise vorticity results for variation in airfoil angle-of-attack.
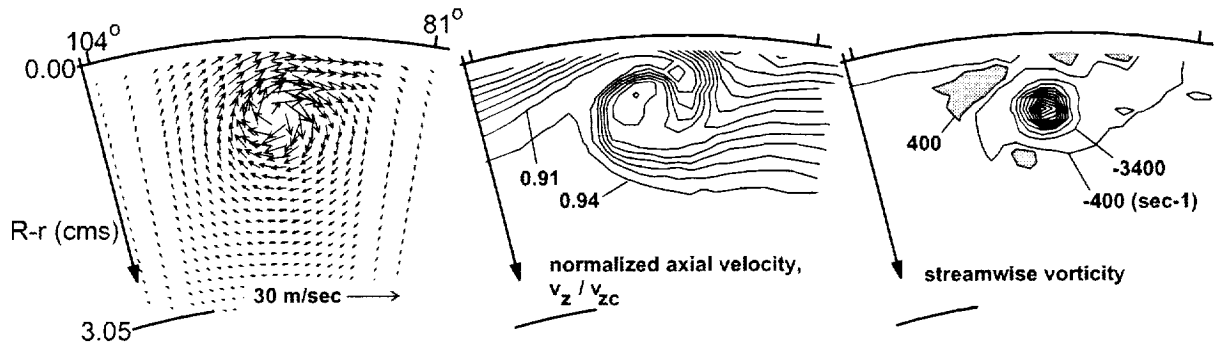
a) Mach = 0.250, circulation = -0.722 m2/sec, peak vorticity = -35714 sec-1
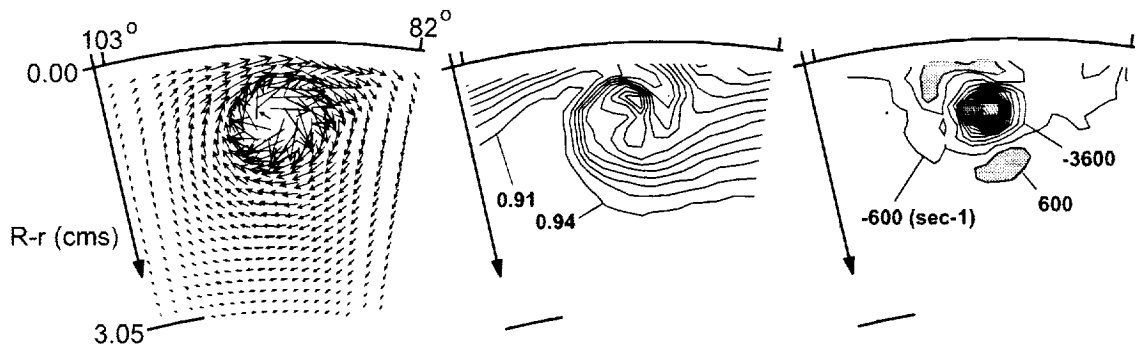
b) Mach = 0.400, circulation = -1.149 m2/sec, peak vorticity = -56831 sec-1
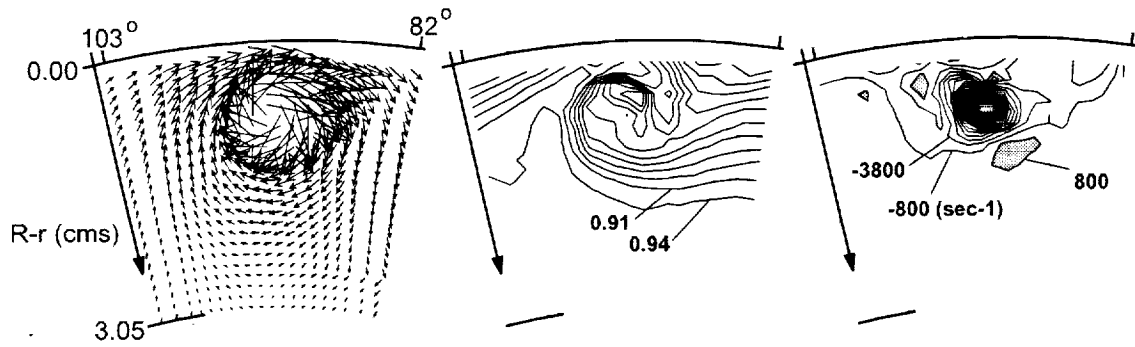
c) Mach = 0.600, circulation = -1.724 m2/sec, peak vorticity = -84000 sec-1

Figure 12 - Velocity and streamwise vorticity results for variation in pipe core Mach number.

a) span = 0.21 cms, circulation = -0.156 m2/sec, peak vorticity = -20297 sec-1

b) span = 0.51 cms, circulation = -0.240 m2/sec, peak vorticity = -22340 sec-1

c) span = 1.02 cms, circulation = -0.253 m2/sec, peak vorticity = -30881 sec-1

d) span = 1.52 cms, circulation = -0.297 m2/sec, peak vorticity = -33368 sec-1

e) span = 2.03 cms, circulation = -0.307 m2/sec, peak vorticity = -38301 sec-1
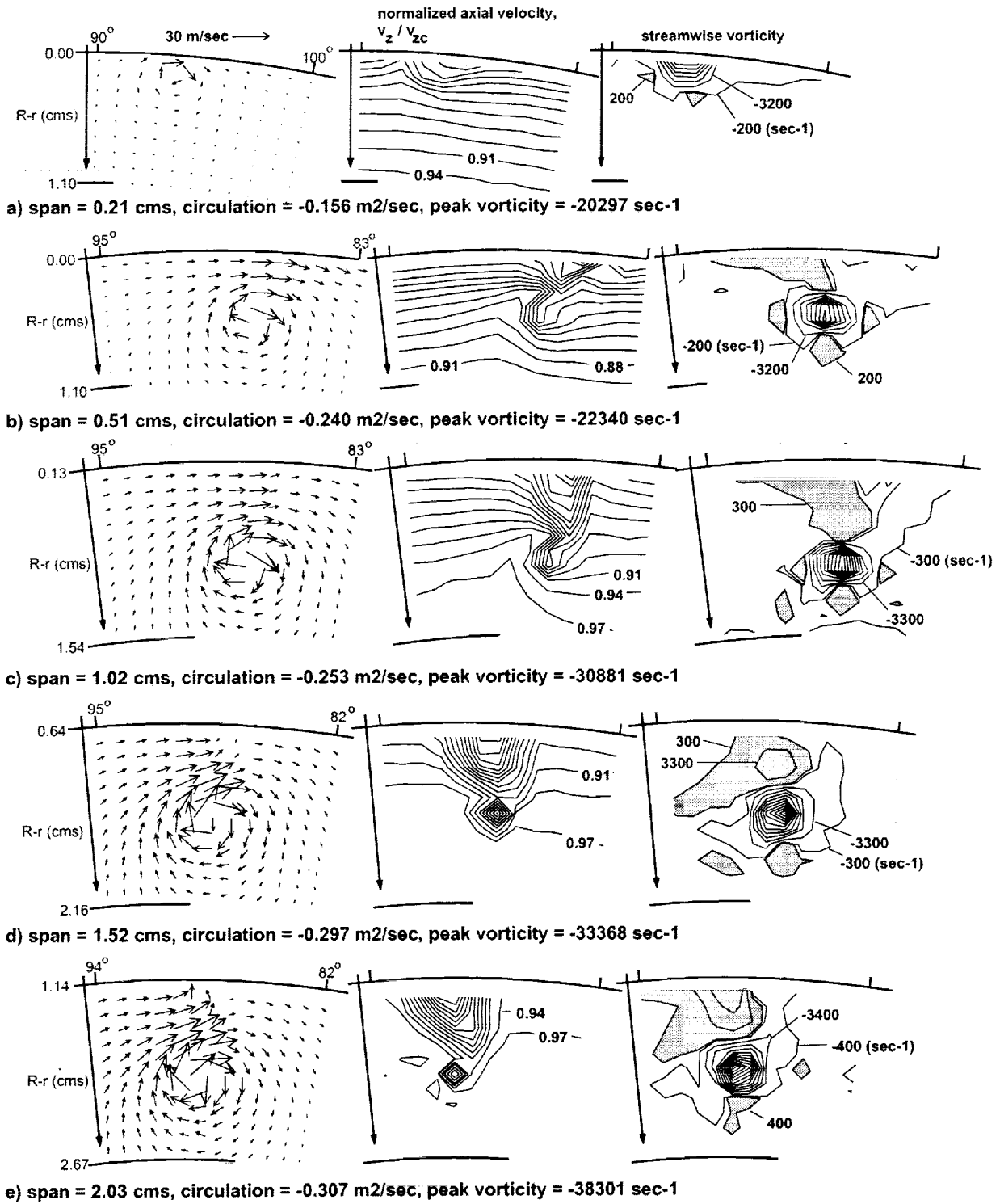
Figure 13 - Velocity and streamwise vorticity results for variation in airfoil span, with chord-length = 0.85 cms.

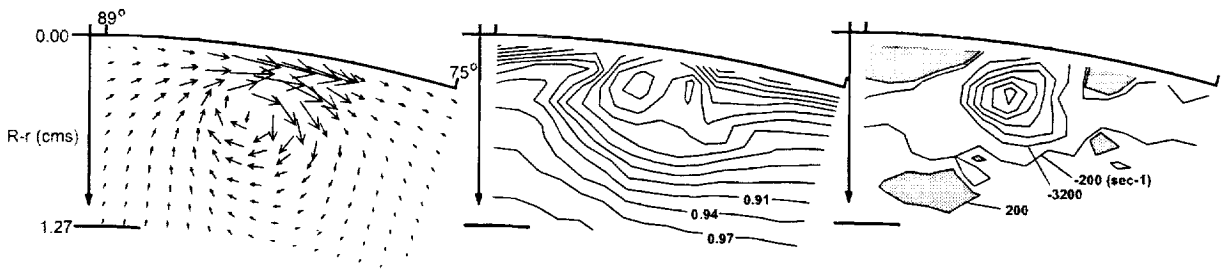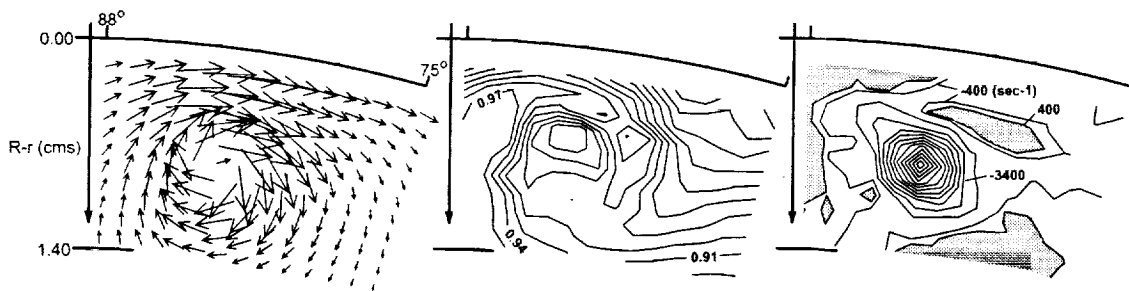a) span = 0.34 cms, circulation = -0.223 m2/sec, peak vorticity = -29194 sec-1

b) span = 0.51 cms, circulation = -0.342 m2/sec, peak vorticity = -23734 sec-1

c) span = 0.81 cms, circulation = -0.315 m2/sec, peak vorticity = -42509 sec-1

d) span = 1.02 cms, circulation = -0.315 m2/sec, peak vorticity = -35415 sec-1

e) span = 1.52 cms, circulation = -0.429 m2/sec, peak vorticity = -37397 sec-1
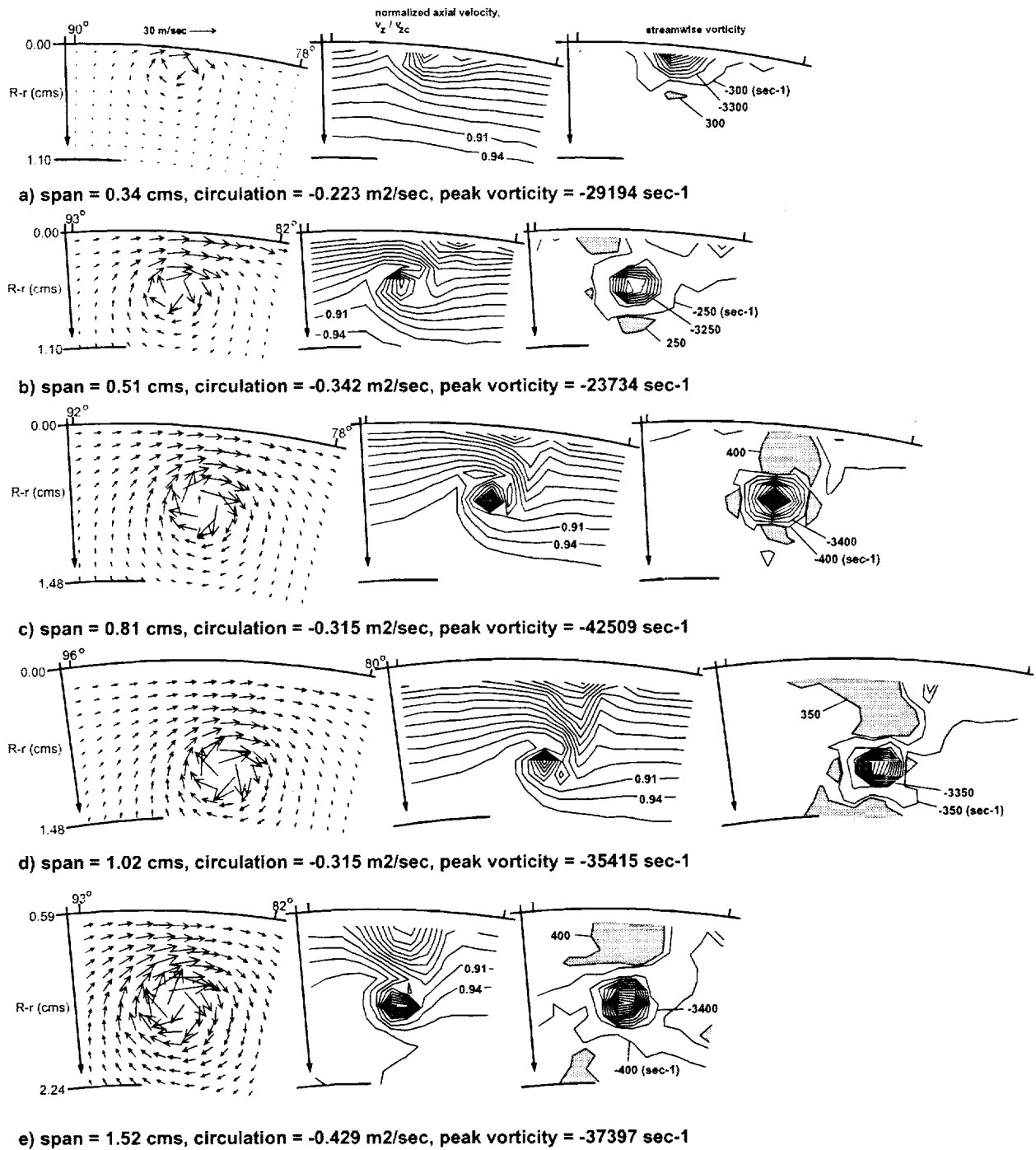
Figure 14 - Velocity and streamwise vorticity results for variation in airfoil span, with chord-length = 1.36 cms.
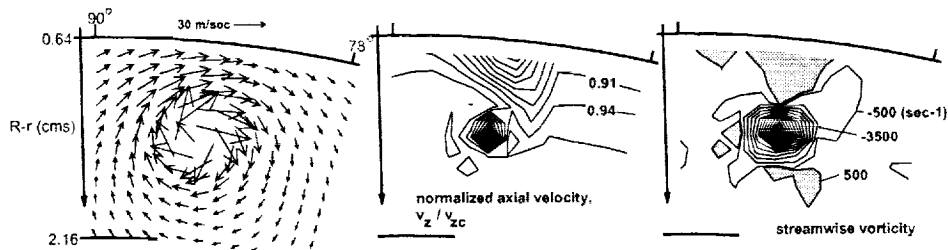
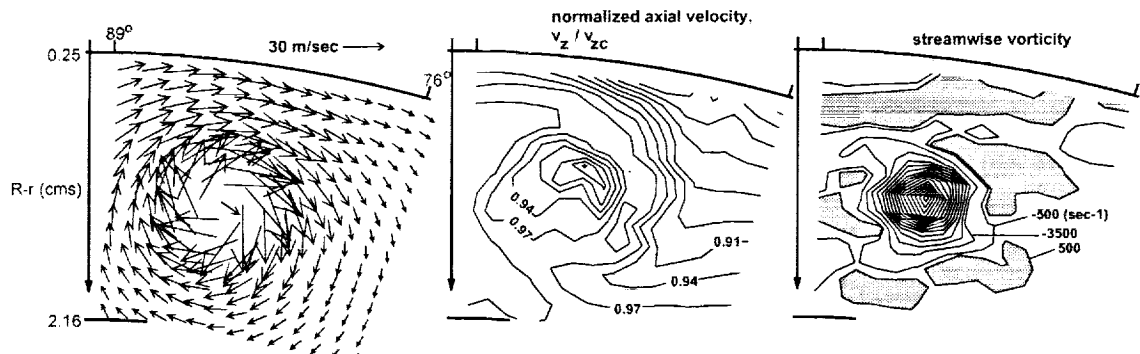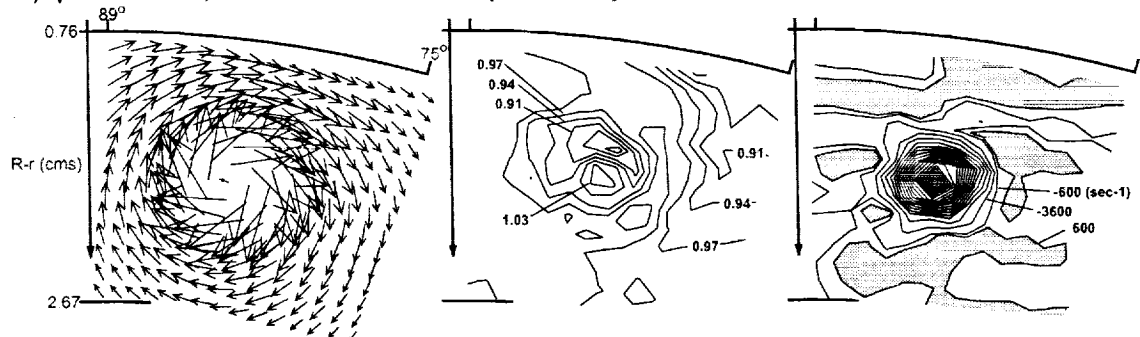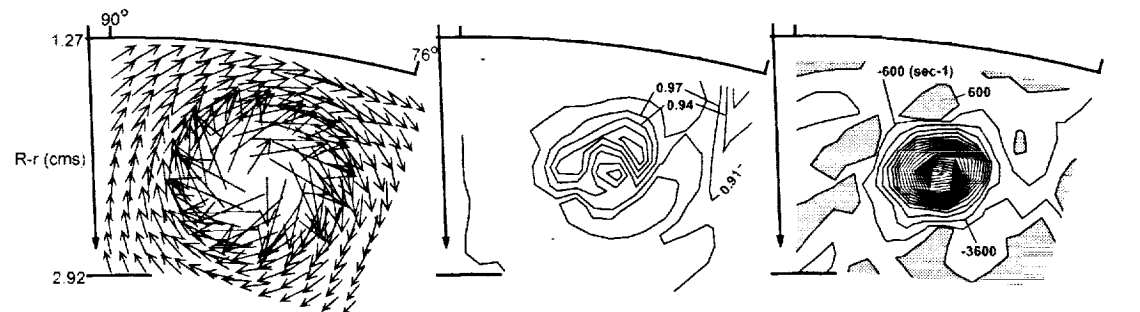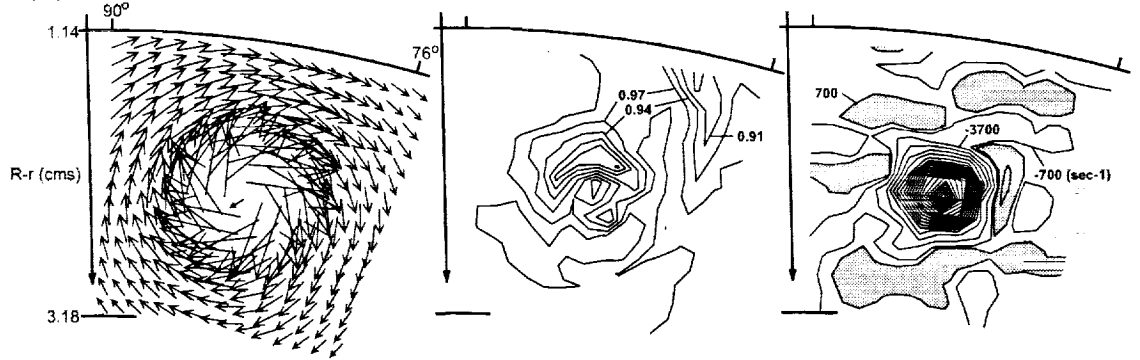f) span = 1.63 cms, circulation = -0.419 m2/sec, peak vorticity = -52295 sec-1
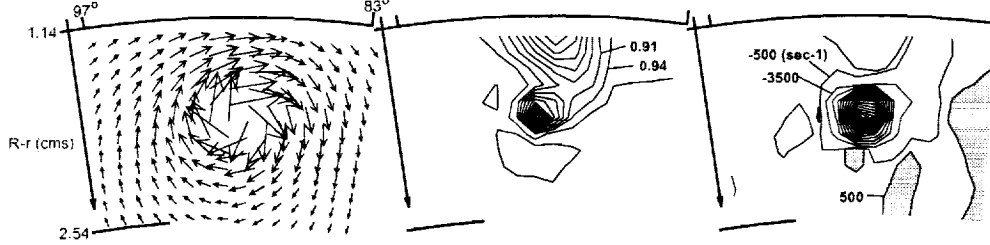
g) span = 2.03 cms, circulation = -0.485 m2/sec, peak vorticity = -50676 sec-1
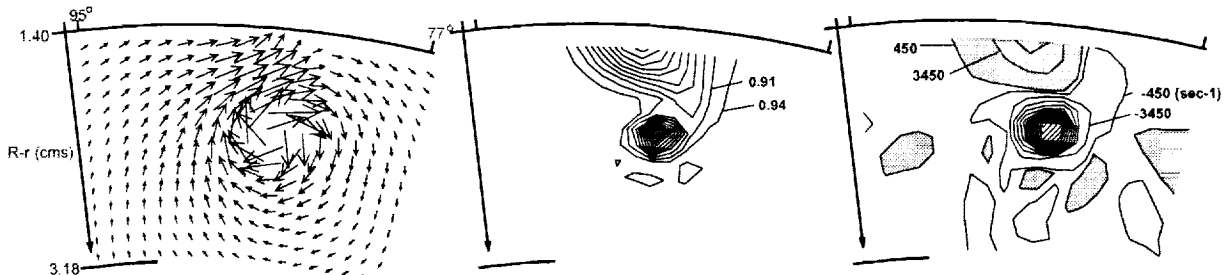
h) span = 2.54 cms, circulation = -0.428 m2/sec, peak vorticity = -44093 sec-1
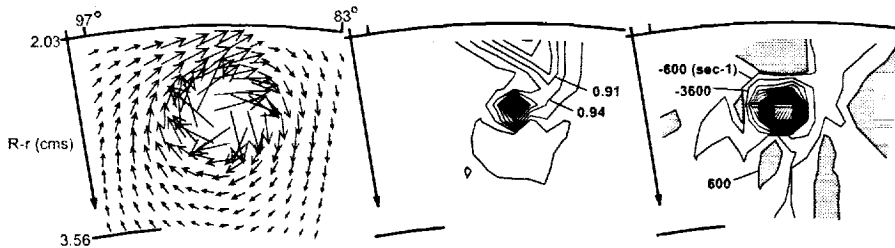
i) span = 3.05 cms, circulation = -0.476 m2/sec, peak vorticity = -60375 sec-1
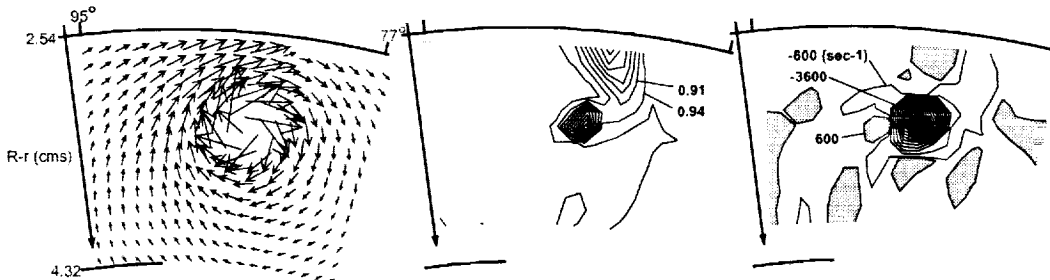
j) span = 3.56 cms, circulation = -0.446 m2/sec, peak vorticity = -63832 sec-1

Figure 14 (continued) - Velocity and streamwise vorticity results for variation in airfoil span, with chord-length = 1.36 cms.

a) span = 0.51 cms, circulation = -0.322 m2/sec, peak vorticity = -27772 sec-1

b) span = 1.02 cms, circulation = -0.435 m2/sec, peak vorticity = -43956 sec-1

c) span = 1.22 cms, circulation = -0.493 m2/sec, peak vorticity = -52181 sec-1

d) span = 1.52 cms, circulation = -0.552 m2/sec, peak vorticity = -57278 sec-1

e) span = 2.03 cms, circulation = -0.596 m2/sec, peak vorticity = -56235 sec-1
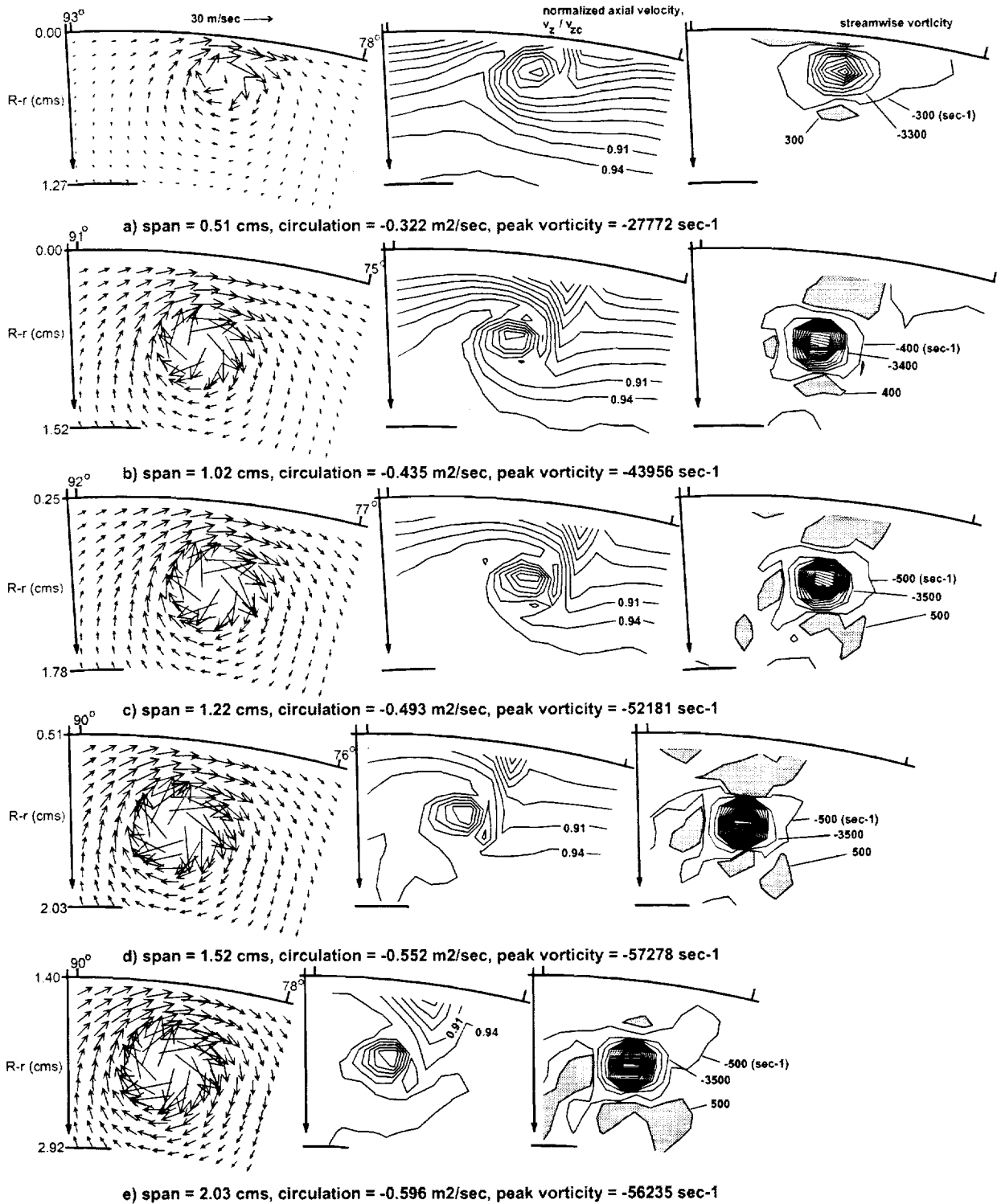
Figure 15 - Velocity and streamwise vorticity results for variation in airfoil span, with chord-length = 2.03 cms.
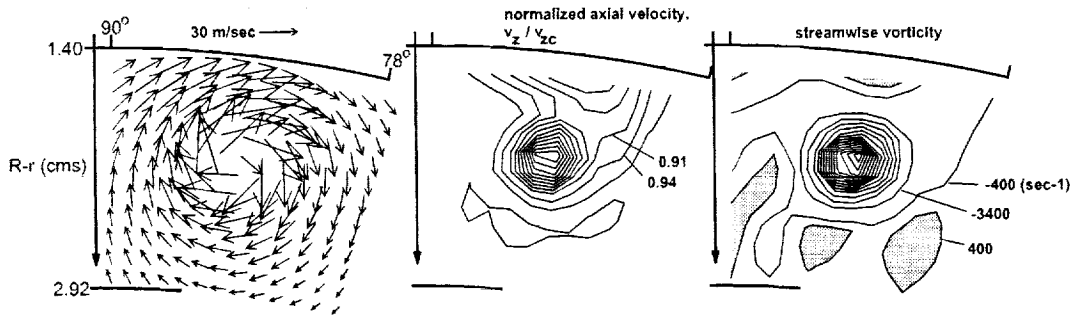
f) span = 2.44 cms, circulation = -0.667 m2/sec, peak vorticity = -44619 sec-1
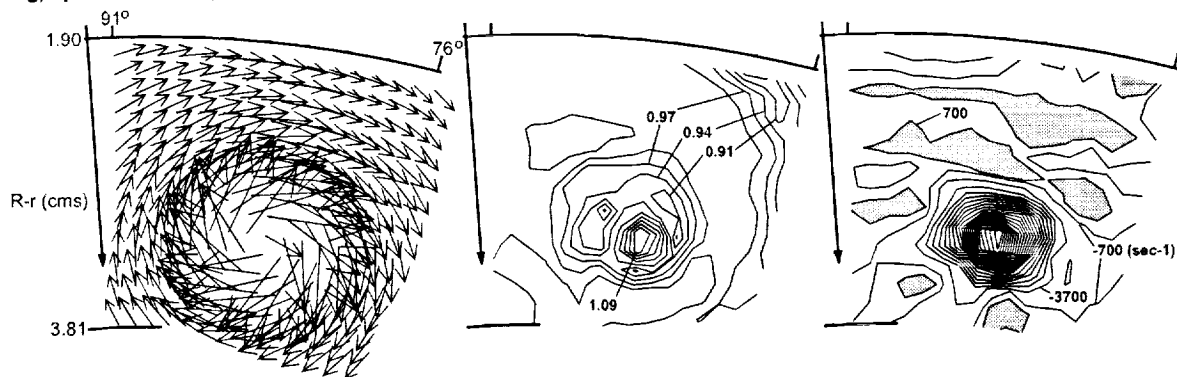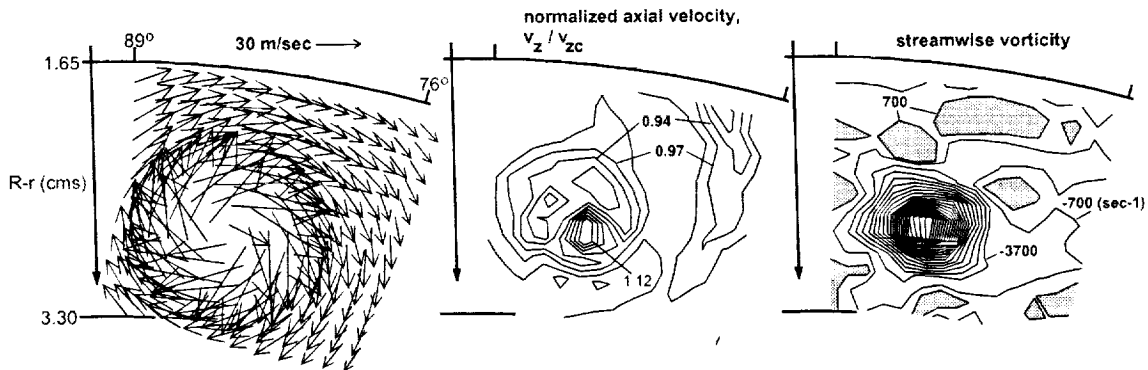
Figure 15 (continued) - Velocity and streamwise vorticity results for variation in airfoil span, with chord-length = 2.03 cms.
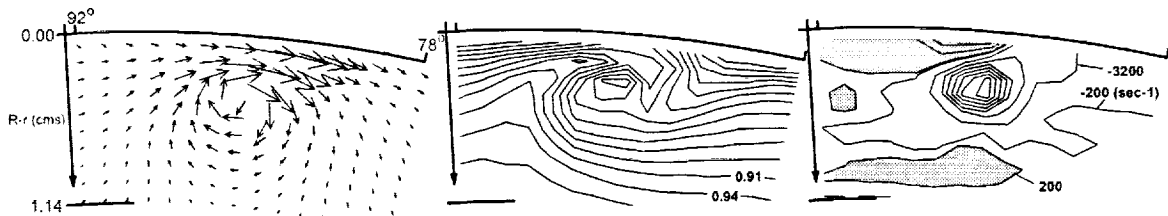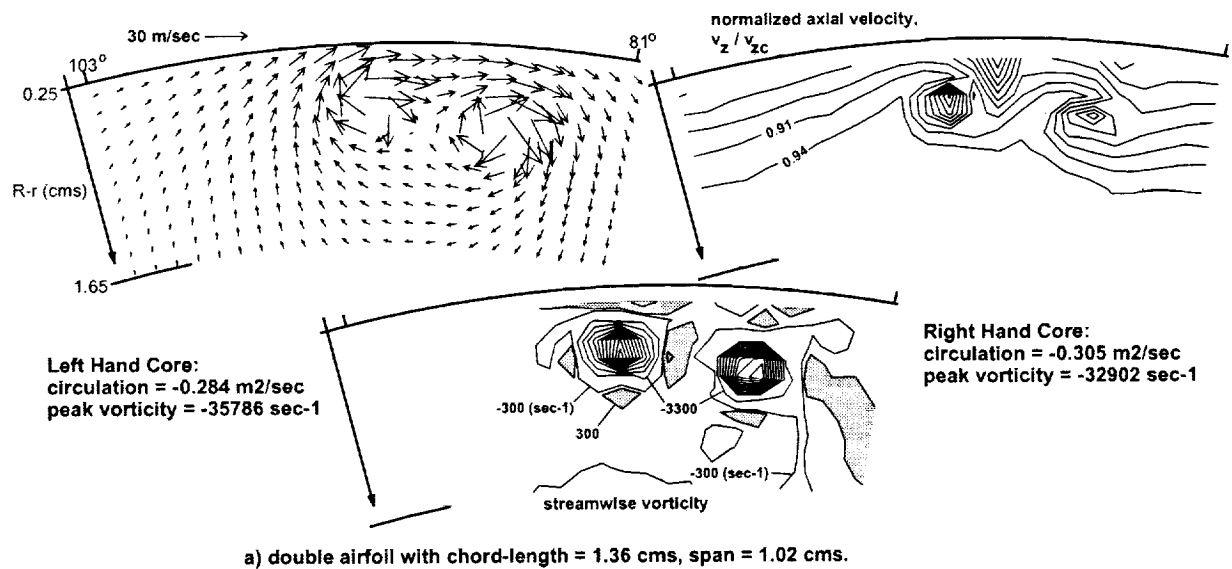
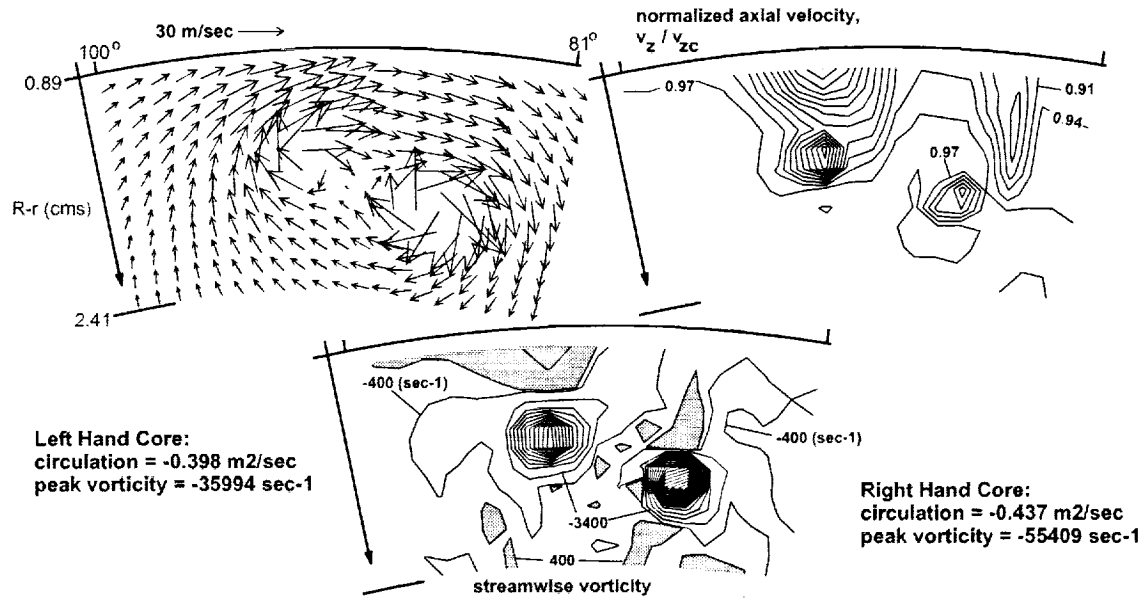a) span = 0.51 cms, circulation = -0.450 m2/sec, peak vorticity = -22914 sec-1
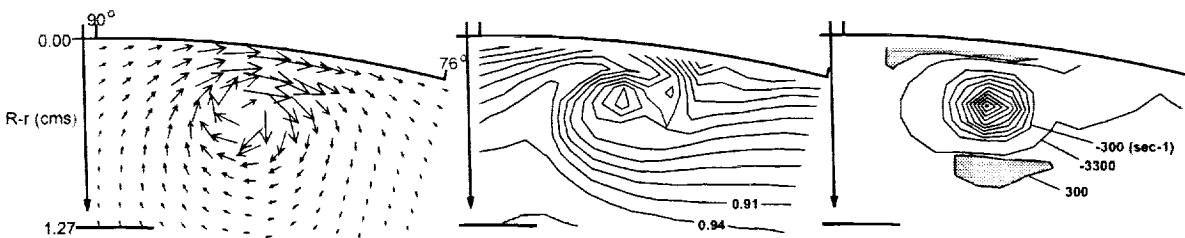
b) span = 0.64 cms, circulation = -0.421 m2/sec, peak vorticity = -31387 sec-1
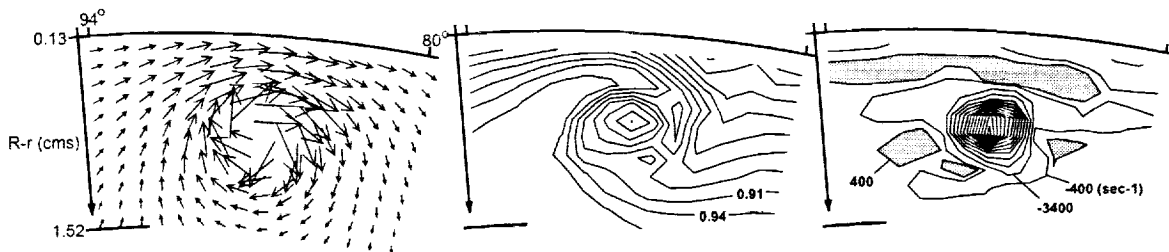
c) span = 1.02 cms, circulation = -0.525 m2/sec, peak vorticity = -43913 sec-1

Figure 16 - Velocity and streamwise vorticity results for variation in airfoil span, with chord-length = 2.54 cms.

d) span = 1.52 cms, circulation = -0.626 m2/sec, peak vorticity = -57104 sec-1

e) span = 2.03 cms, circulation = -0.719 m2/sec, peak vorticity = -73333 sec-1

f) span = 2.54 cms, circulation = -0.781 m2/sec, peak vorticity = 58750 sec-1

g) span = 3.05 cms, circulation = -0.825 m2/sec, peak vorticity = -42748 sec-1

h) span = 3.56 cms, circulation = -0.862 m2/sec, peak vorticity = -46882
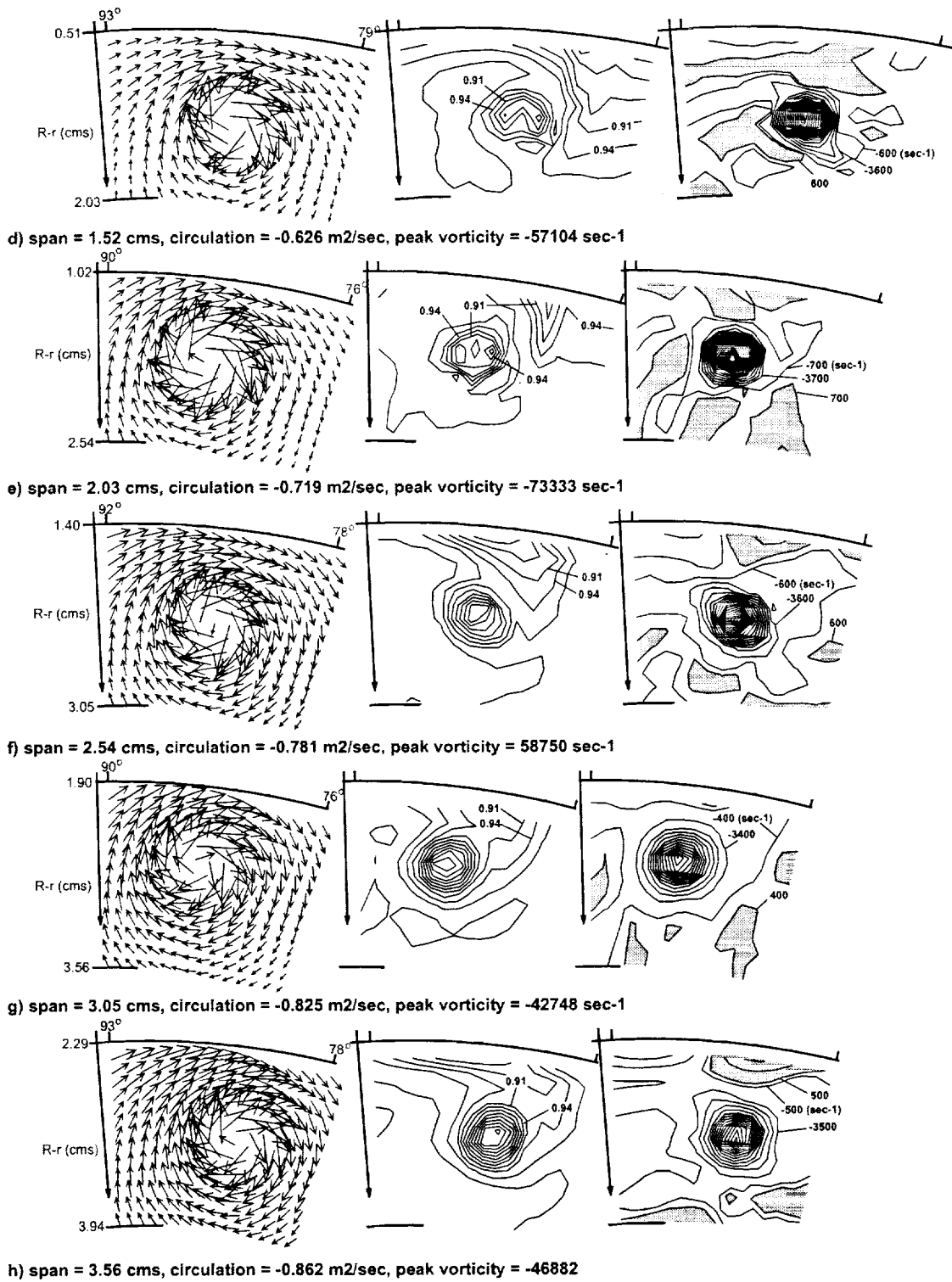
Figure 16 (continued) - Velocity and streamwise vorticity results for variation in airfoil span, with chord-length = 2.54 cms.
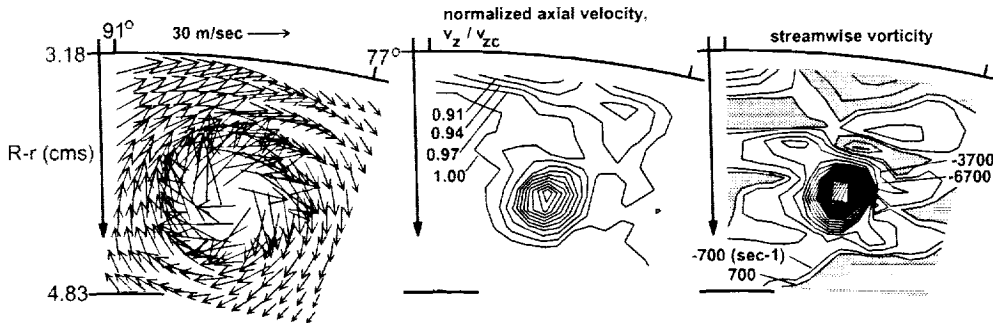
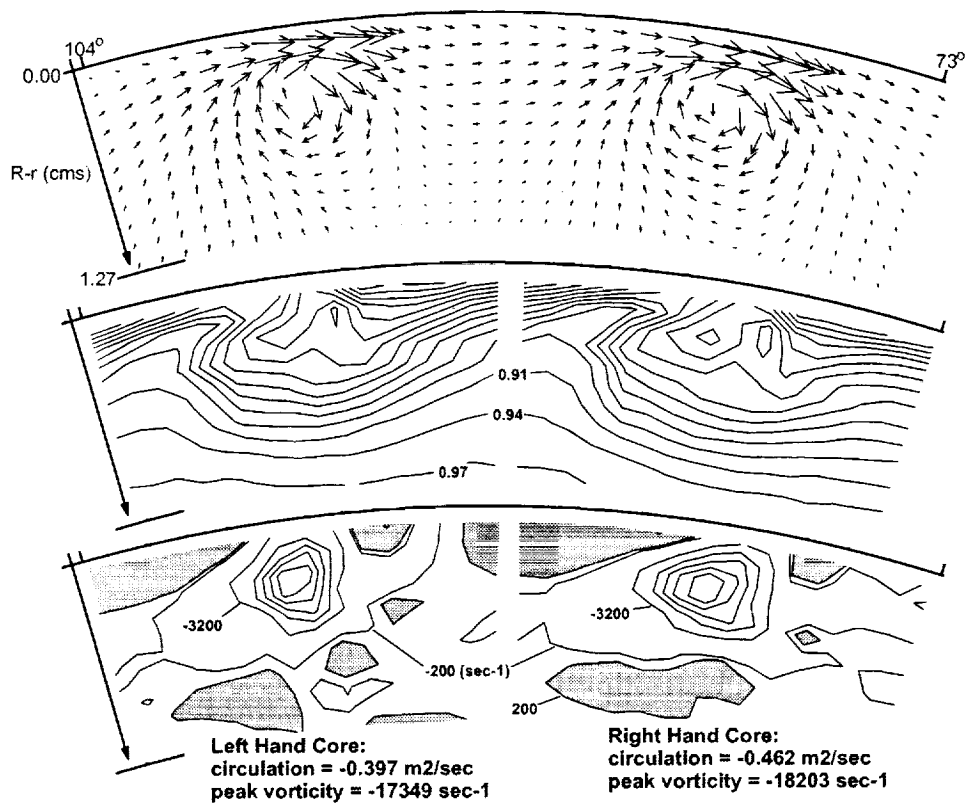i) span = 4.57 cms, circulation = -0.866 m2/sec, peak vorticity = -70289 sec-1

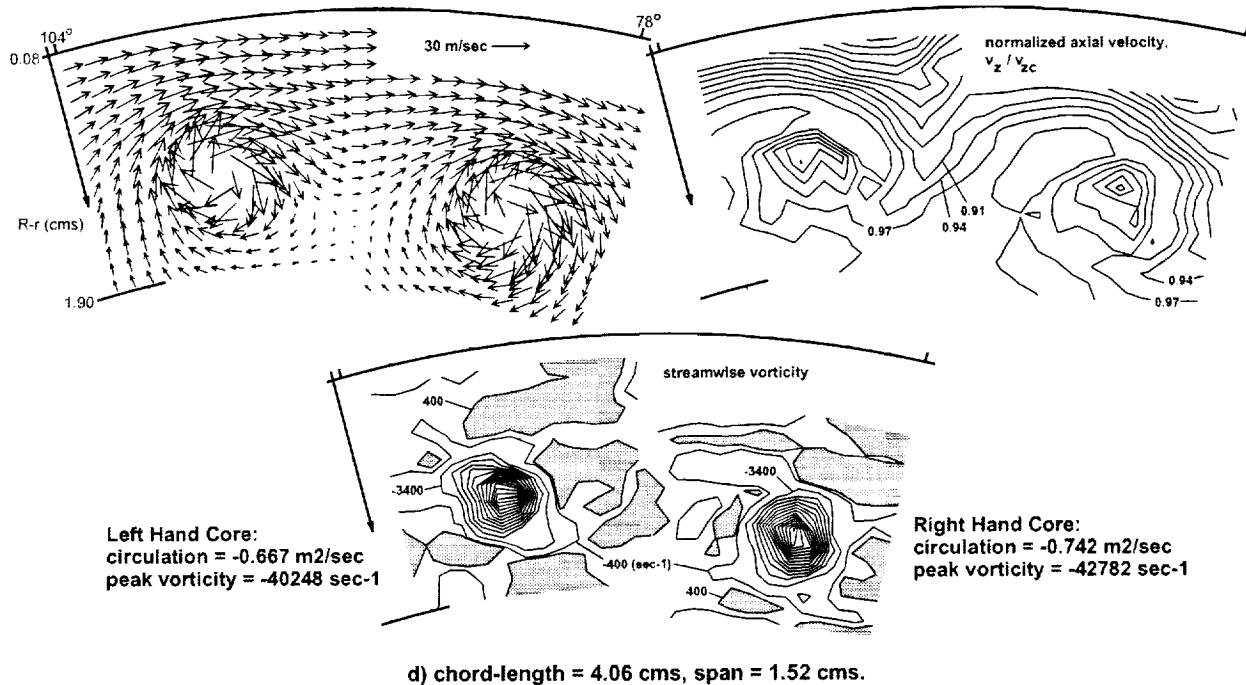Figure 16 (continued) - Velocity and streamwise vorticity results for variation in airfoil span, with chord-length = 2.54 cms.
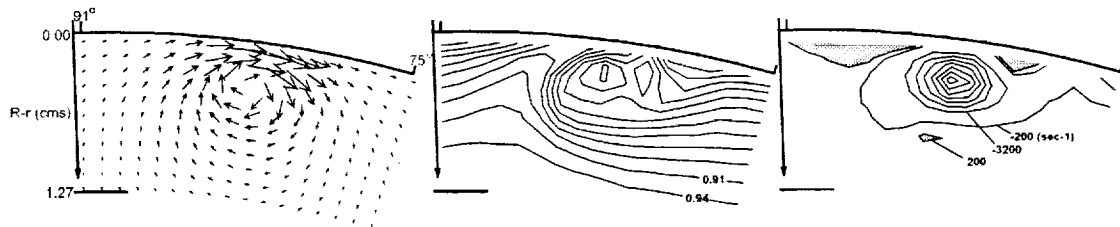
a) span = 0.51 cms, circulation = -0.399 m2/sec, peak vorticity = -23345 sec-1
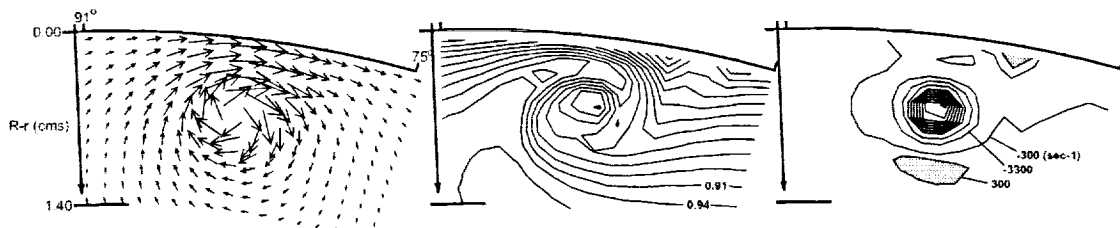
b) span = 0.76 cms, circulation = -0.530 m2/sec, peak vorticity = -30924 sec-1
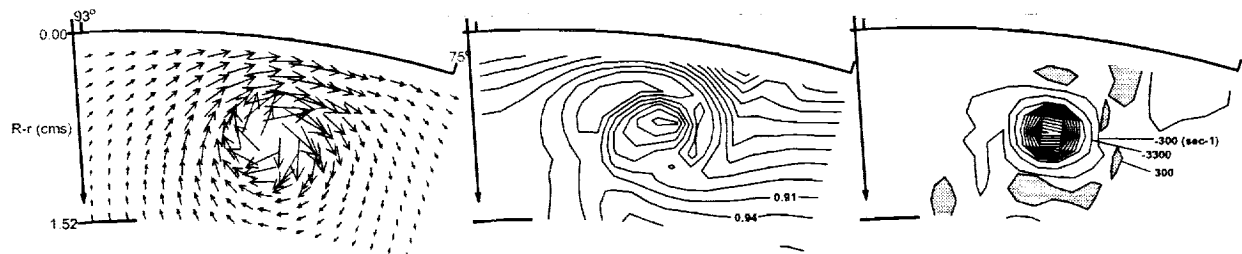
c) span = 1.02 cms, circulation = -0.591 m2/sec, peak vorticity = -40099 sec-1

Figure 17 - Velocity and streamwise vorticity results for variation in airfoil span, with chord-length = 3.05 cms.
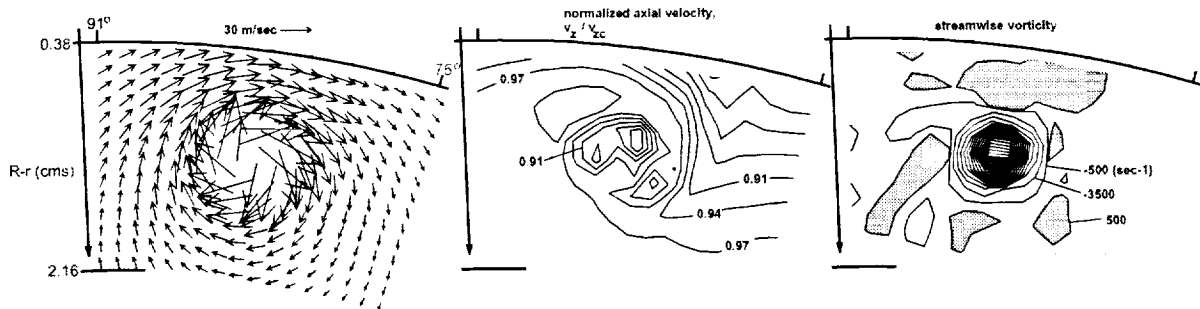
d) span = 1.52 cms, circulation = -0.704 m2/sec, peak vorticity = -53251 sec-1

e) span = 1.83 cms, circulation = -0.776 m2/sec, peak vorticity = -59852 sec-1
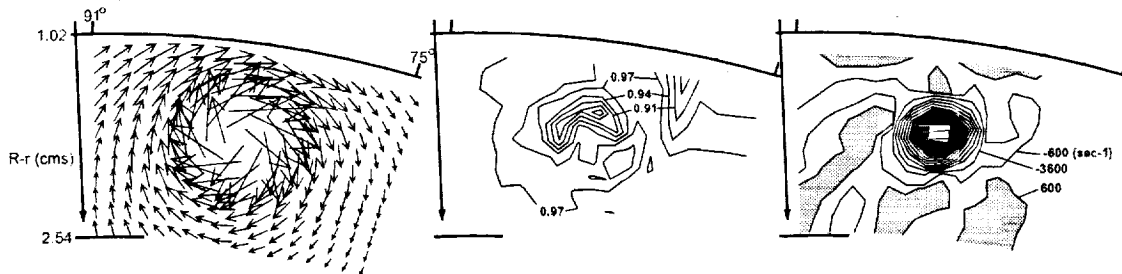
f) span = 2.03 cms, circulation = -0.817 m2/sec, peak vorticity = -58695 sec-1

g) span = 3.66 cms, circulation = -0.985 m2/sec, peak vorticity = -35505 sec-1

Figure 17 (continued) - Velocity and streamwise vorticity results for variation in airfoil span, with chord-length = 3.05 cms.

a) span = 0.51 cms, circulation = -0.451 m2/sec, peak vorticity = -21114 sec-1

b) span = 0.89 cms, circulation = -0.662 m2/sec, peak vorticity = -36897 sec-1

c) span = 1.02 cms, circulation = -0.648 m2/sec, peak vorticity = -40085 sec-1

d) span = 1.52 cms, circulation = -0.780 m2/sec, peak vorticity = -54079 sec-1

e) span = 2.03 cms, circulation = -0.944 m2/sec, peak vorticity = -59439 sec-1
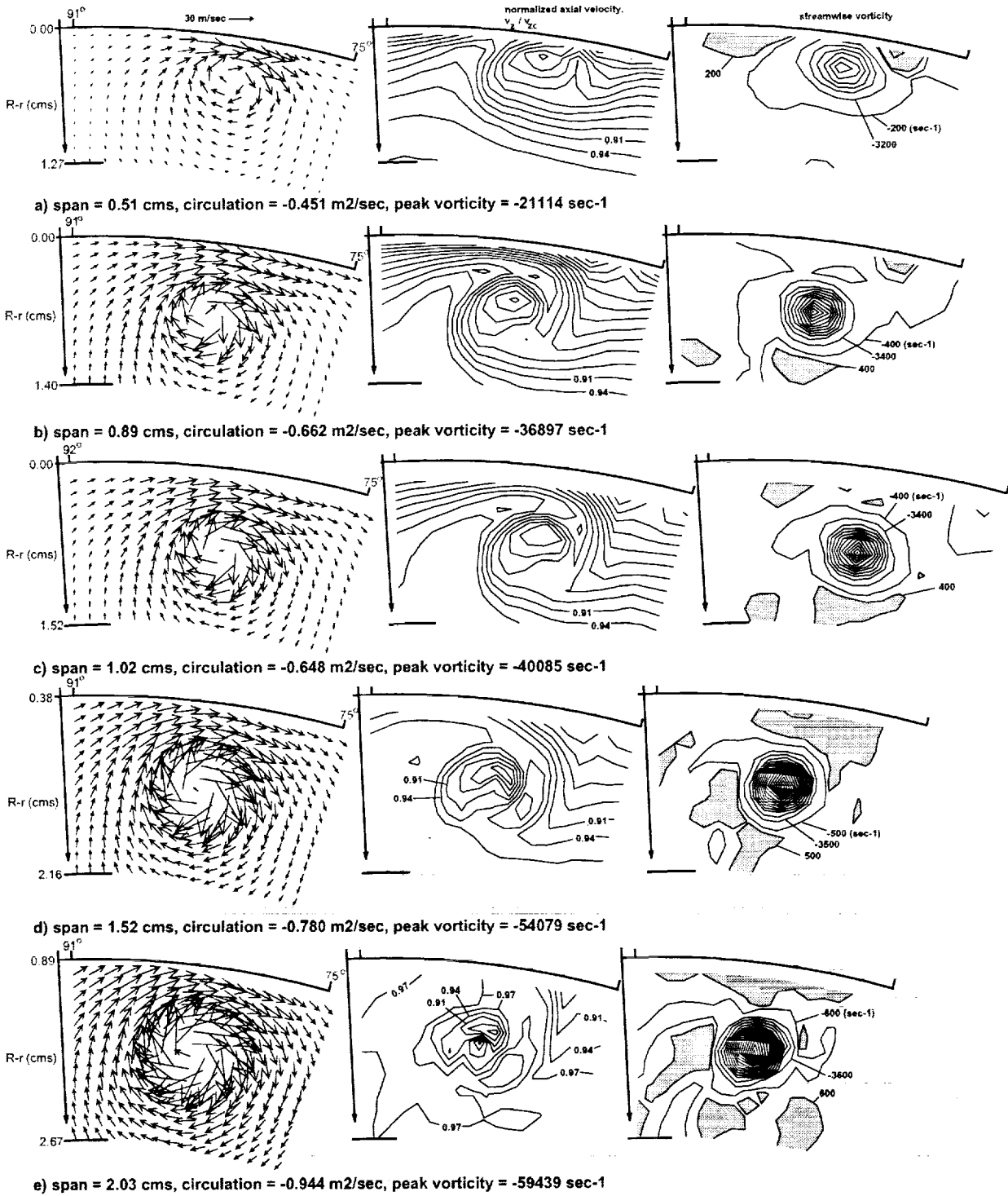
Figure 18 - Velocity and streamwise vorticity results for variation in airfoil span, with chord-length = 3.56 cms.
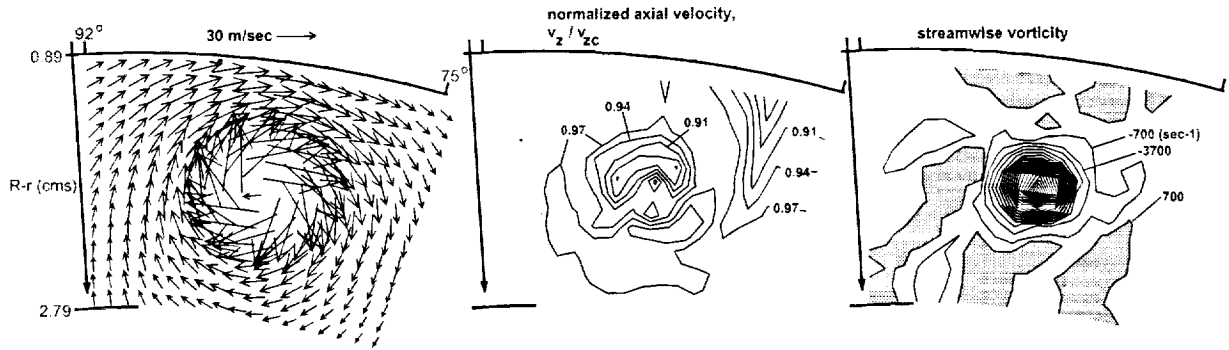
f) span = 2.13 cms, circulation = -0.941 m2/sec, peak vorticity = -67331 sec-1
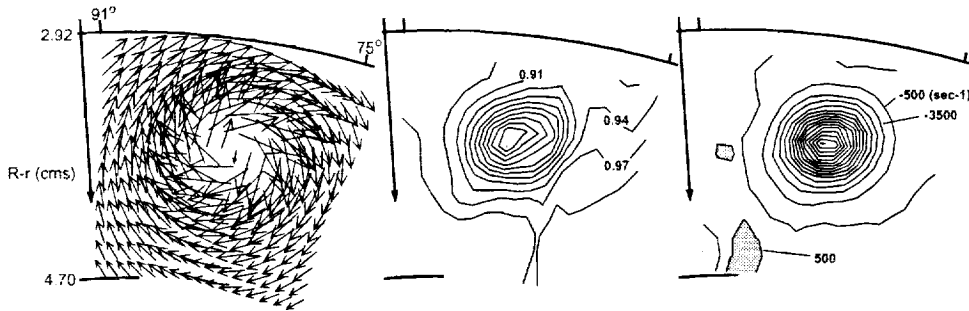
g) span = 4.27 cms, circulation = -1.170 m2/sec, peak vorticity = -45710 sec-1

Figure 18 (continued) - Velocity and streamwise vorticity results for variation in airfoil span, with chord-length = 3.56 cms.

a) span = 0.51 cms, circulation = -0.429 m2/sec, peak vorticity = -19956 sec-1

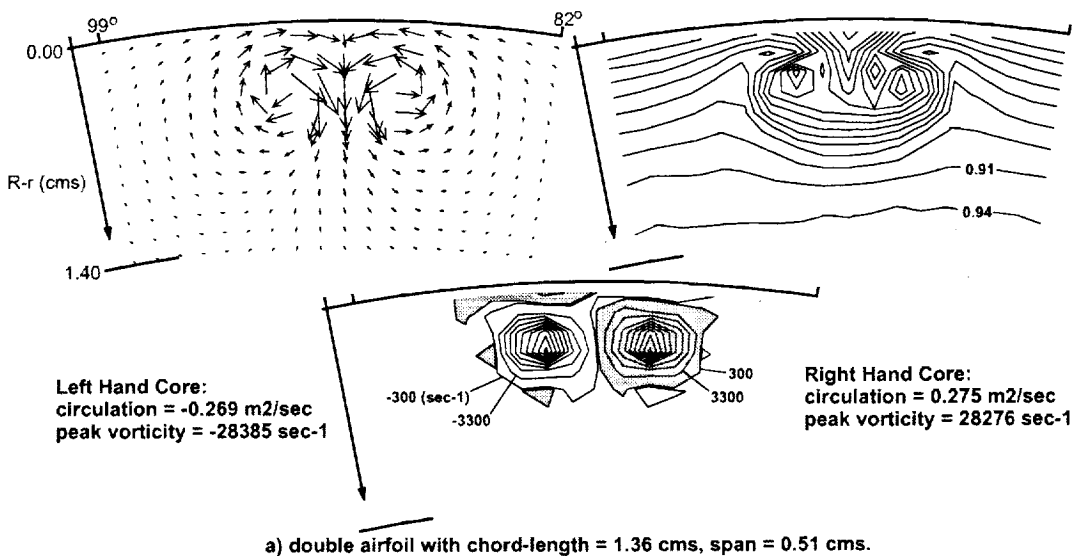b) span = 1.02 cms, circulation = -0.713 m2/sec, peak vorticity = -39161 sec-1

Figure 19 - Velocity and streamwise vorticity results for variation in airfoil span, with chord-length = 4.06 cms.

c) span = 1.52 cms, circulation = -0.824 m2/sec, peak vorticity = -50476 sec-1

d) span = 2.03 cms, circulation = -0.961 m2/sec, peak vorticity = -60834 sec-1

e) span = 2.44 cms, circulation = -1.044 m2/sec, peak vorticity = -63493 sec-1

f) span = 2.54 cms, circulation = -1.045 m2/sec, peak vorticity = -66113 sec-1

Figure 19 (continued) - Velocity and streamwise vorticity results for variation in airfoil span, with chord-length = 4.06 cms.

g) span = 3.05 cms, circulation = -1.210 m2/sec, peak vorticity = -66124 sec-1

h) span = 3.56 cms, circulation = -1.243 m2/sec, peak vorticity = -69638 sec-1

Figure 19 (continued) - Velocity and streamwise vorticity results for variation in airfoil span, with chord-length = 4.06 cms.

Left Hand Core:
circulation = -0.284 m2/sec
peak vorticity = -35786 sec-1

Right Hand Core:
circulation = -0.305 m2/sec
peak vorticity = -32902 sec-1

a) double airfoil with chord-length = 1.36 cms, span = 1.02 cms.

Figure 20 - Velocity and streamwise vorticity results for airfoil pairs shedding co-rotating vortices.

30 m/sec ⟶

normalized axial velocity, v_z / v_{zc}

Left Hand Core:
circulation = -0.398 m2/sec
peak vorticity = -35994 sec-1

Right Hand Core:
circulation = -0.437 m2/sec
peak vorticity = -55409 sec-1

streamwise vorticity

b) double airfoil with chordlength = 1.36 cms, span = 2.03 cms.

Left Hand Core:
circulation = -0.397 m2/sec
peak vorticity = -17349 sec-1

Right Hand Core:
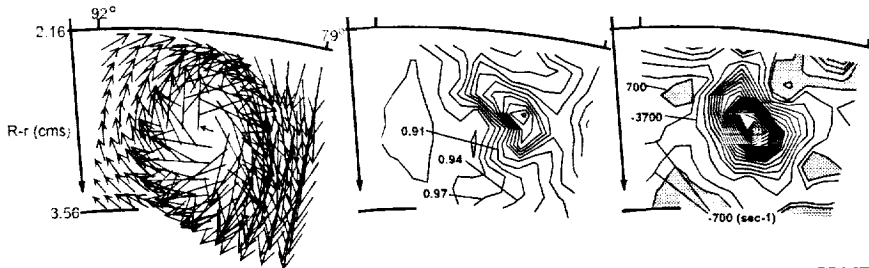circulation = -0.462 m2/sec
peak vorticity = -18203 sec-1

c) chord-length = 4.06 cms, span = 0.51 cms.

Figure 20 (continued) - Velocity and streamwise vorticity results for airfoil pairs shedding co-rotating vortices.

Left Hand Core:
circulation = -0.667 m2/sec
peak vorticity = -40248 sec-1

Right Hand Core:
circulation = -0.742 m2/sec
peak vorticity = -42782 sec-1

d) chord-length = 4.06 cms, span = 1.52 cms.

Left Hand Core:
circulation = -0.879 m2/sec
peak vorticity = -48733 sec-1

Right Hand Core:
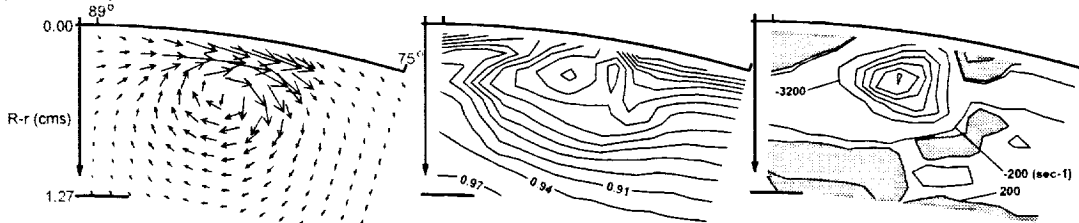circulation = -0.954 m2/sec
peak vorticity = -55171 sec-1

e) chord-length = 4.06 cms, span = 2.54 cms.
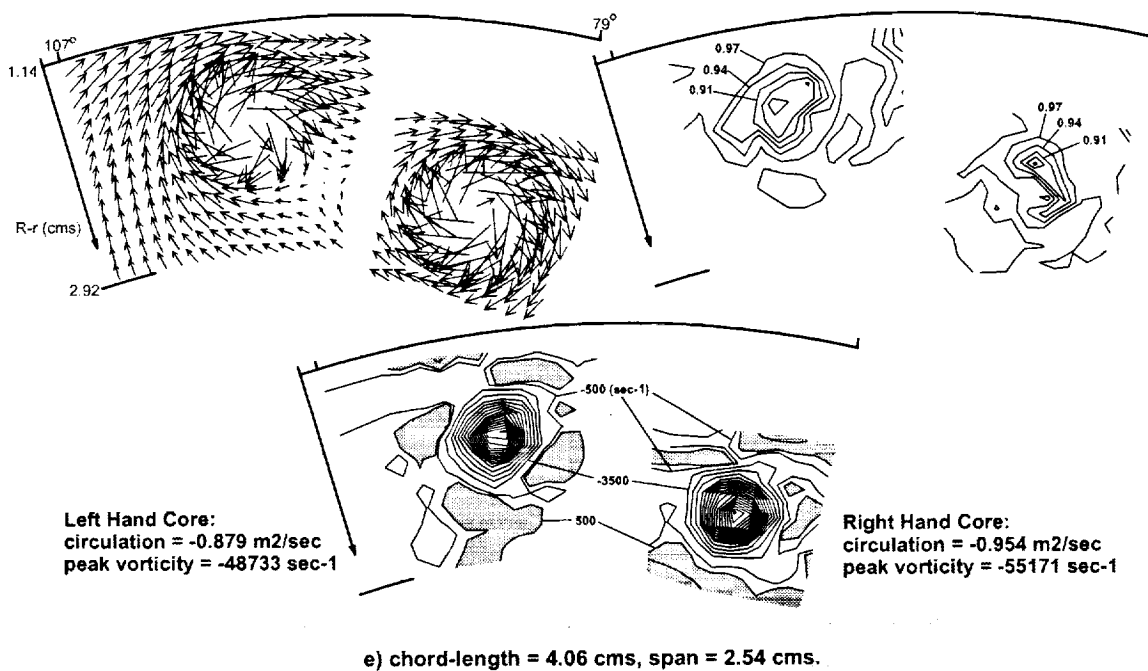
Figure 20 (continued) - Velocity and streamwise vorticity results for airfoil pairs shedding co-rotating vortices.
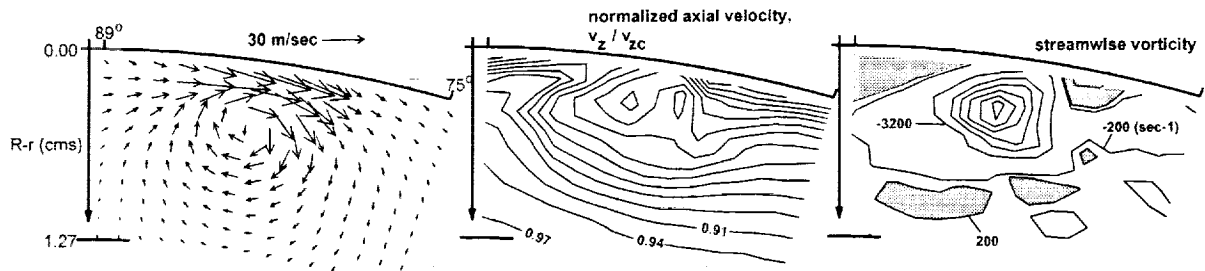
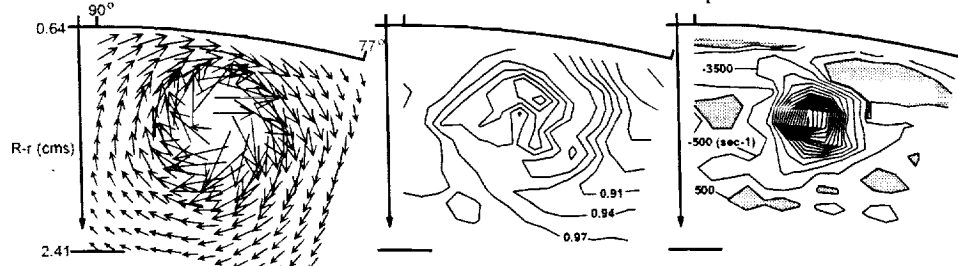f) right hand core, chord-length = 4.06 cms, span = 0.51 cms, circulation = -0.482 m2/sec, peak vorticity = -19853 sec-1
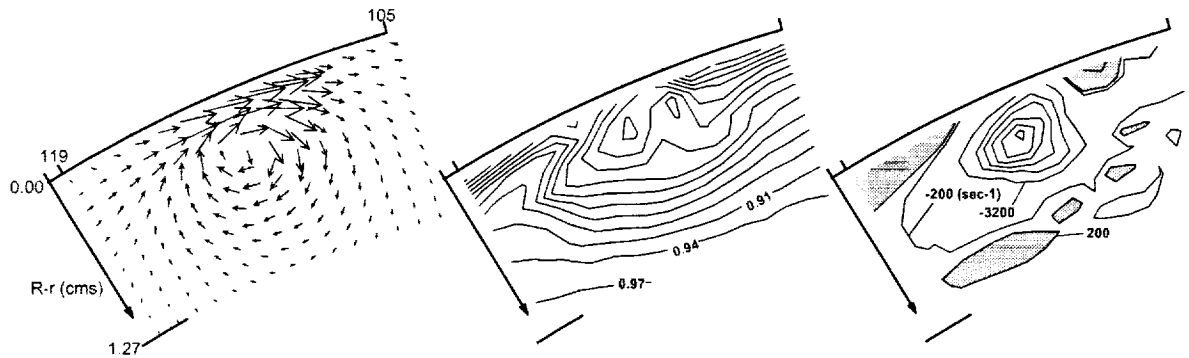
g) left hand core, chord-length = 4.06 cms, span = 0.51 cms, circulation = -0.480 m2/sec, peak vorticity = -19411 sec-1
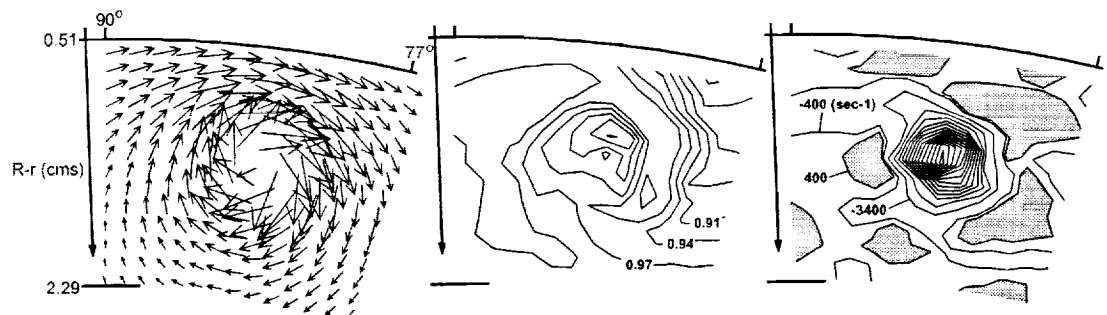
h) right hand core, chord-length = 4.06 cms, span = 1.52 cms, circulation = -0.794 m2/sec, peak vorticity = -43568 sec-1
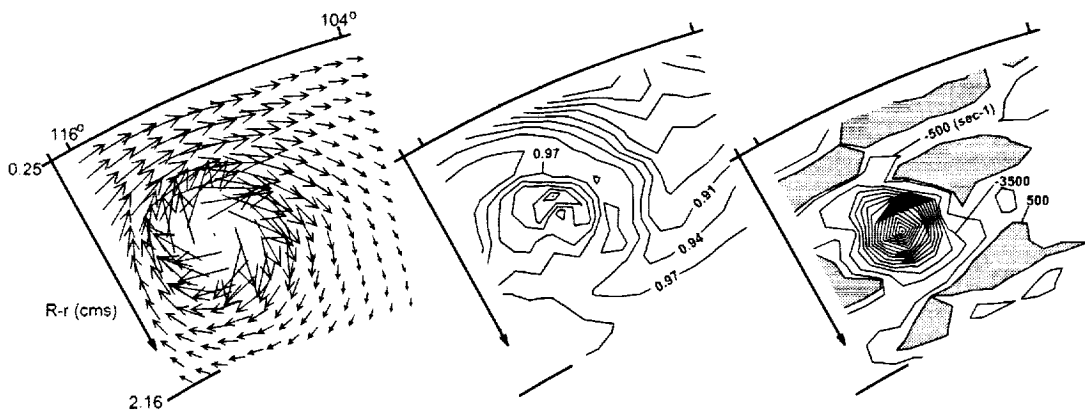
i) left hand core, chord-length = 4.06 cms, span = 1.52 cms, circulation = -0.794 m2/sec, peak vorticity = -49131 sec-1

Figure 20 (continued) Velocity and streamwise vorticity results for airfoil pairs shedding co-rotating vortices.
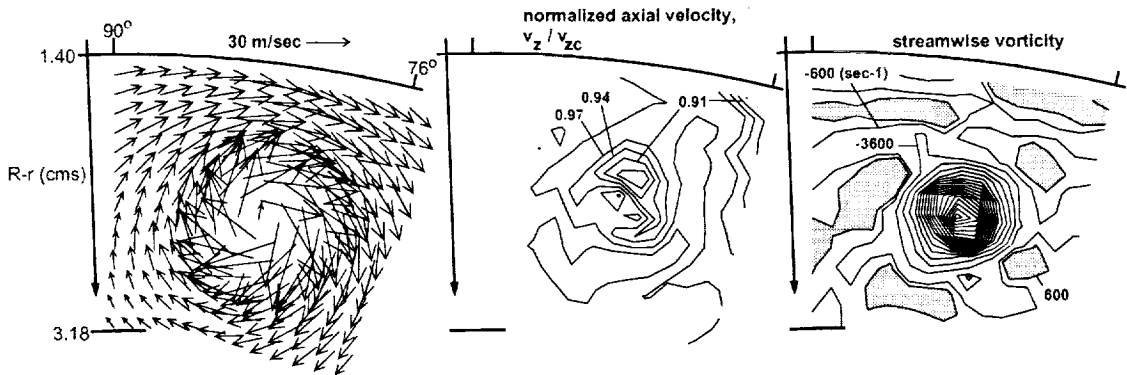
j) right hand core, chord-length = 4.06 cms, span = 2.54 cms, circulation = -1.012 m2/sec, peak vorticity = -56314 sec-1
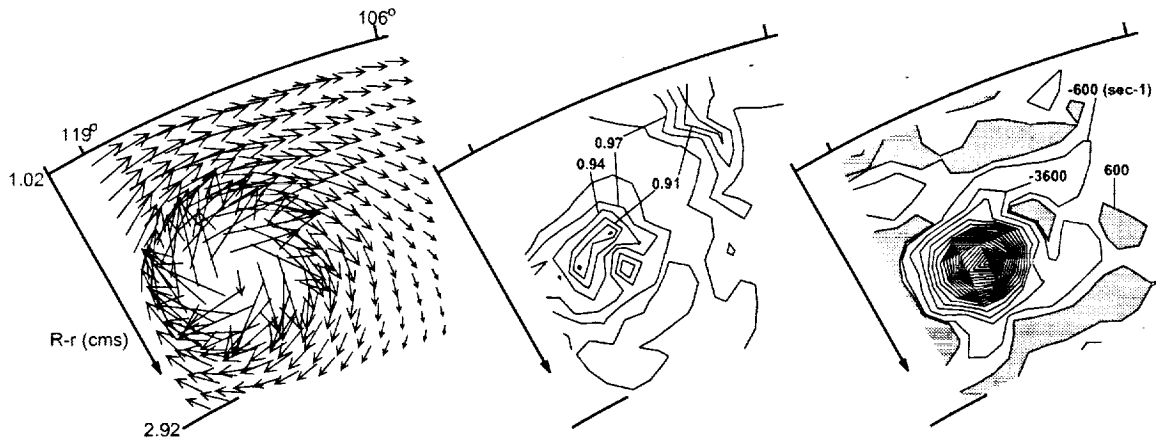
k) left hand core, chord-length = 4.06 cms, span = 2.54 cms, circulation = -1.021 m2/sec, peak vorticity = -62701 sec-1
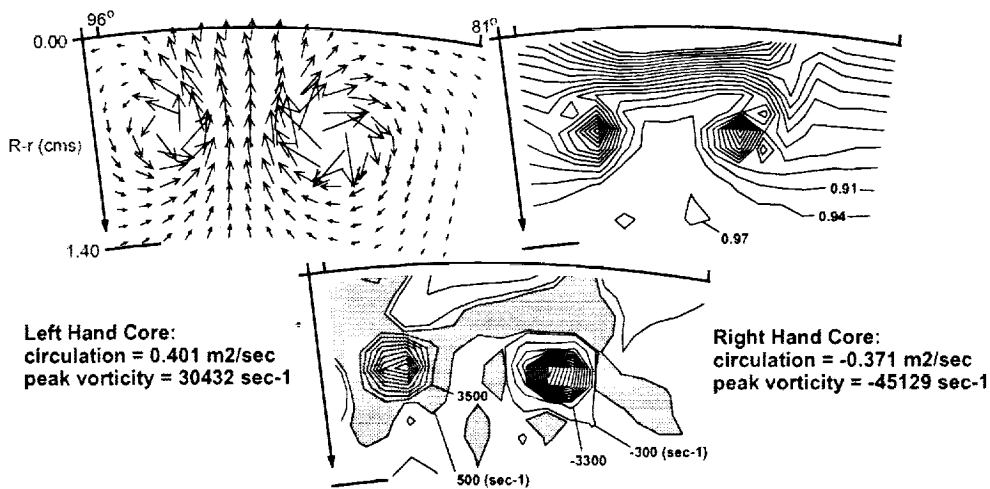
Figure 20 (continued) - Velocity and streamwise vorticity results for airfoil pairs shedding co-rotating vortices.

Left Hand Core:
circulation = -0.269 m2/sec
peak vorticity = -28385 sec-1

Right Hand Core:
circulation = 0.275 m2/sec
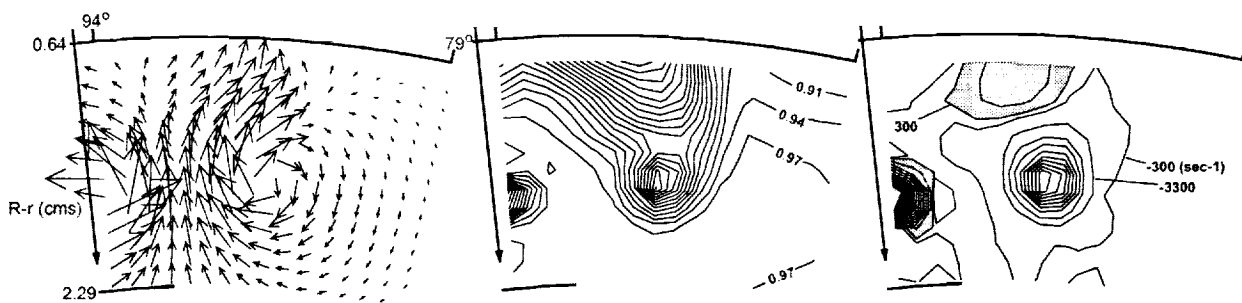peak vorticity = 28276 sec-1

a) double airfoil with chord-length = 1.36 cms, span = 0.51 cms.

Figure 21 - Velocity and streamwise vorticity results for airfoil pairs shedding counter-rotating up vortices.

normalized axial velocity,
v_z / v_{zc}

Left Hand Core:
circulation = -0.402 m2/sec
peak vorticity = -36723 sec-1

Right Hand Core:
circulation = 0.403 m2/sec
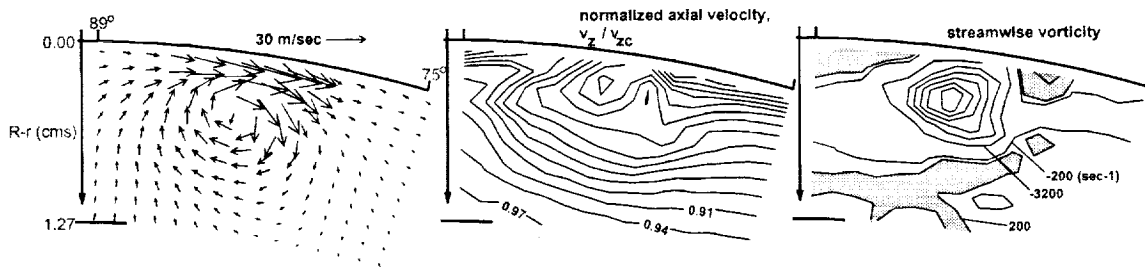peak vorticity = 40026 sec-1

streamwise vorticity
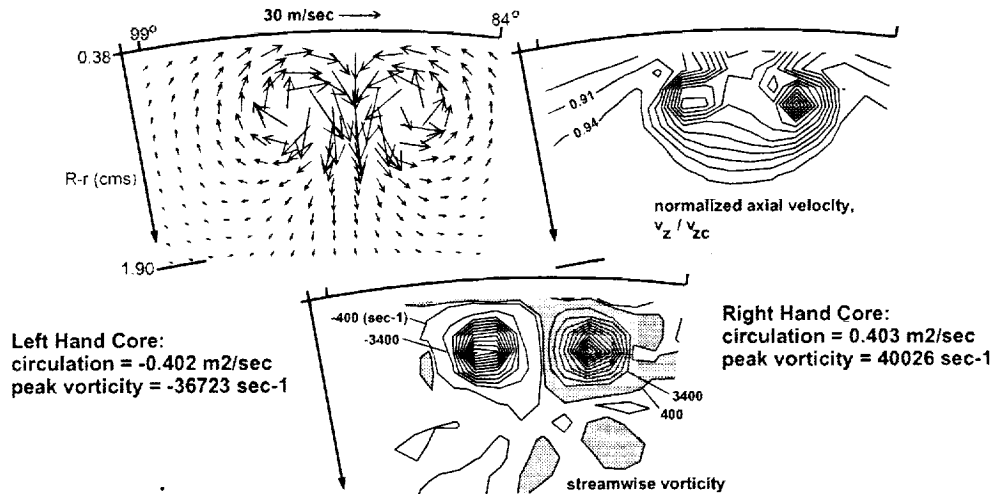
b) double airfoil with chord-length = 1.36 cms, span = 1.02 cms.
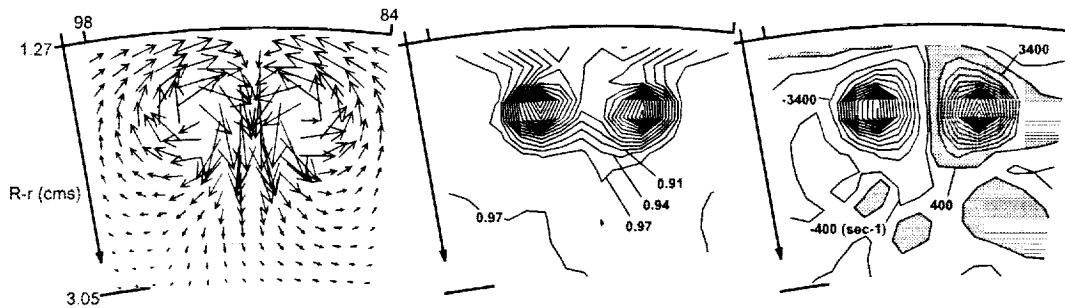
c) double airfoil with chord-length = 1.36 cms, span = 2.03 cms,
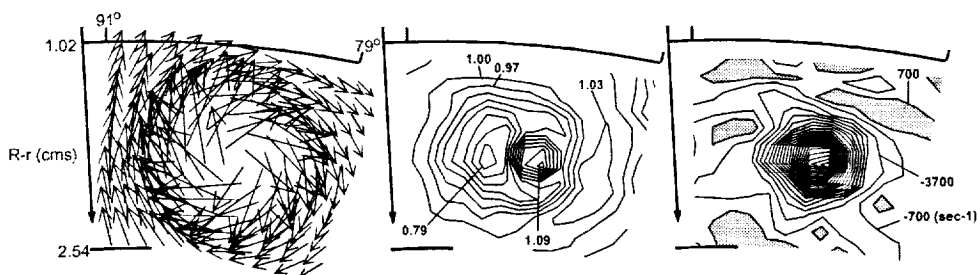left hand core: circulation = -0.567 m2/sec, peak vorticity = -39639 sec-1,
right hand core: circulation = 0.545 m2/sec, peak vorticity = 45039 sec-1.
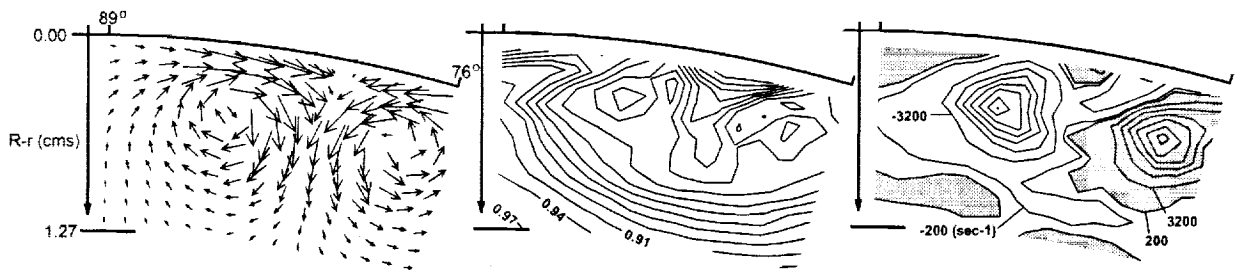
d) chord-length = 4.06 cms, span = 0.51 cms,
left hand core: circulation = -0.580 m2/sec, peak vorticity = -21634 sec-1
right hand core: circulation > 0.422 m2/sec, peak vorticity = 19828 sec-1.

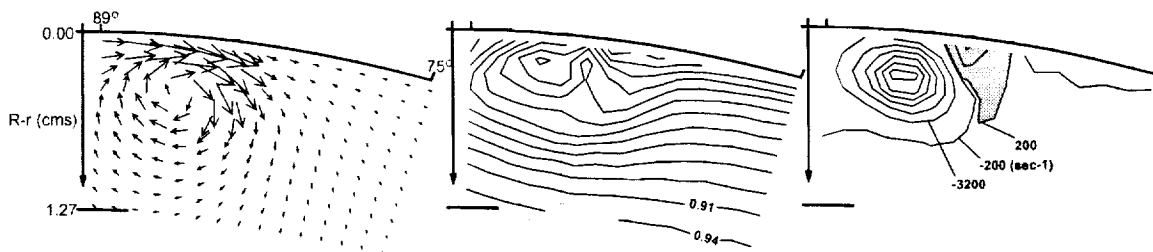Figure 21 (continued) - Velocity and streamwise vorticity results for airfoil pairs shedding counter-rotating up vortices.
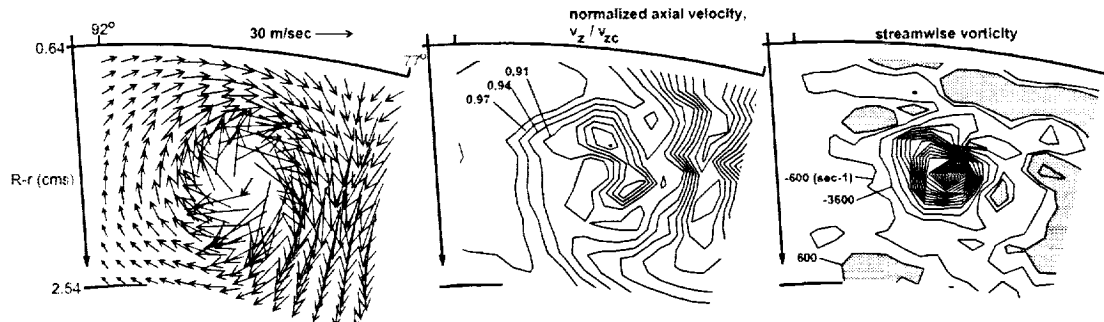
e) chord-length = 4.06 cms, span = 1.52 cms, circulation = -1.120 m2/sec, peak vorticity = -56758 sec-1.

f) chord-length = 4.06 cms, span = 2.54 cms, circulation = -1.340 m2/sec, peak vorticity = -66147 sec-1.

g) chord-length = 4.06 cms, span = 0.51 cms, circulation = -0.499 m2/sec, peak vorticity = -18690 sec-1.

h) chord-length = 4.06 cms, span = 1.52 cms, circulation = -0.916, peak vorticity = -49315 sec-1.
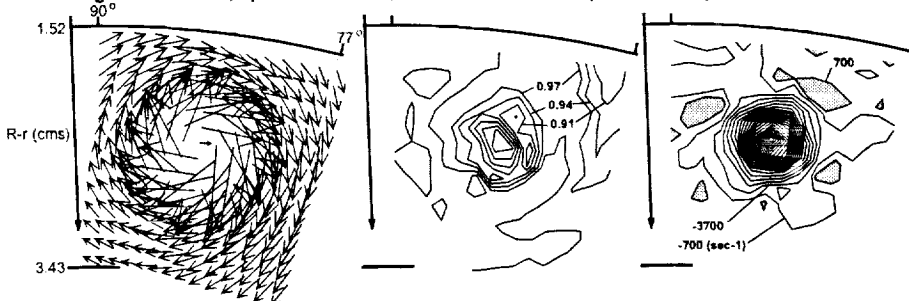
i) chord-length = 4.06 cms, span = 2.54 cms, circulation = -1.201 m2/sec, peak vorticity = -69724 sec-1.

Figure 21 (continued) - Velocity and streamwise vorticity results for airfoil pairs shedding counter-rotating up vortices.

Left Hand Core:
circulation = 0.280 m2/sec
peak vorticity = 29840 sec-1

Right Hand Core:
circulation = -0.290 m2/sec
peak vorticity = -31244 sec-1

a) double airfoil with chord-length = 1.36 cms, span = 0.51 cms.

Left Hand Core:
circulation = 0.401 m2/sec
peak vorticity = 30432 sec-1
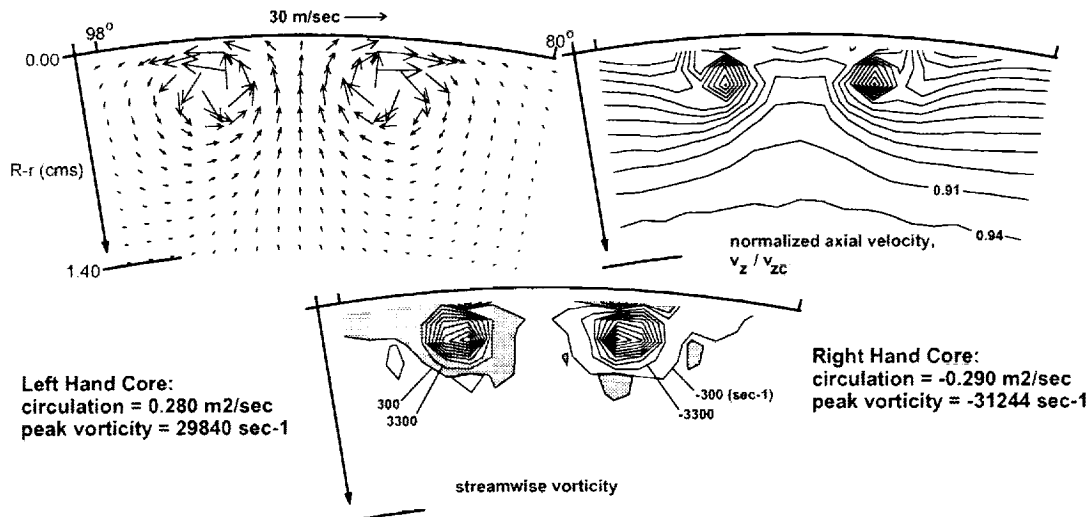
Right Hand Core:
circulation = -0.371 m2/sec
peak vorticity = -45129 sec-1

b) double airfoil with chord-length = 1.36 cms, span = 1.02 cms.

c) double airfoil with chord-length = 1.36 cms, span = 2.03 cms,
right hand core: circulation = -0.494 m2/sec, peak vorticity = -29692 sec-1

Figure 22 - Velocity and streamwise vorticity results for airfoil pairs shedding counter-rotating down vortices.

d) right hand core, chord-length = 4.06 cms, span = 0.51 cms, circulation = -0.516 m2/sec, peak vorticity = -21336 sec-1
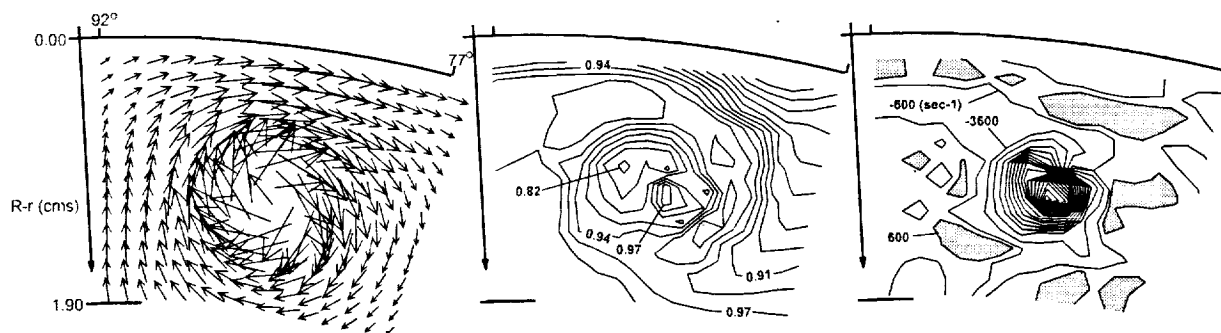
e) right hand core, chord-length = 4.06 cms, span = 1.52 cms, circulation = -1.064 m2/sec, peak vorticity = -56439 sec-1

f) right hand core, chord-length = 4.06 cms, span = 2.54 cms, circulation = -1.326 m2/sec, peak vorticity = -68872 sec-1
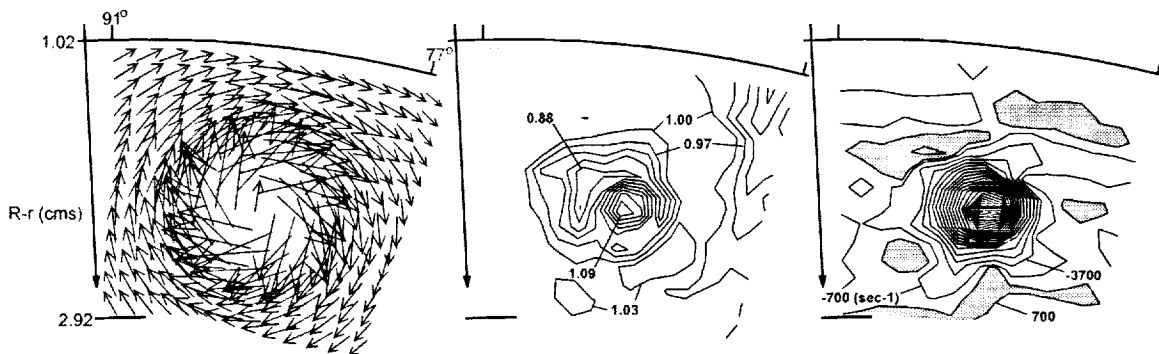
g) right hand core, chord-length = 4.06 cms, span = 0.51 cms, circulation = -0.465 m2/sec, peak vorticity = -19842 sec-1

Figure 22 (continued) - Velocity and streamwise vorticity results for airfoil pairs shedding counter-rotating down vortices.
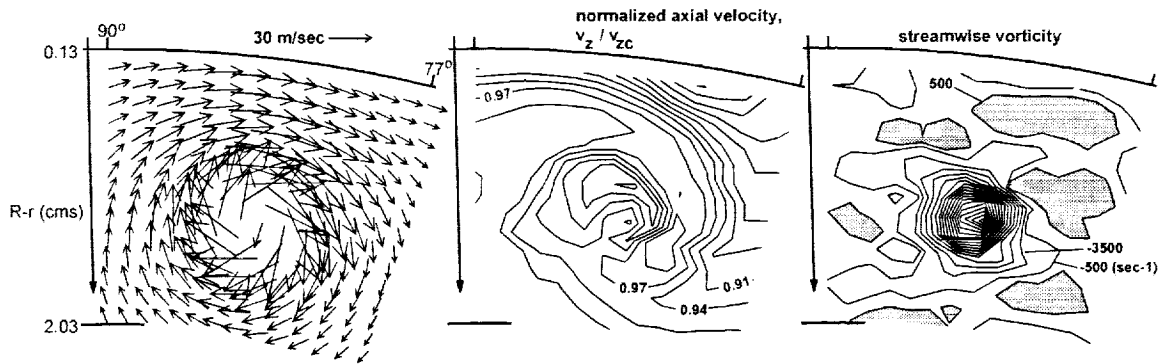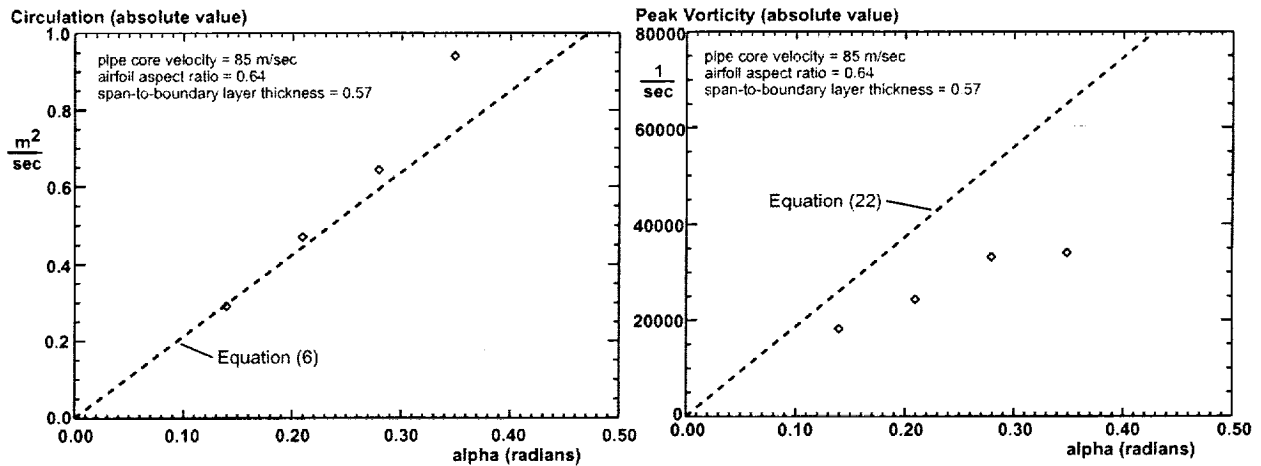
h) right hand core, chord-length = 4.06 cms, span = 1.52 cms, circulation = -0.917 m2/sec, peak vorticity = -53157 sec-1

i) right hand core, chord-length = 4.06 cms, span = 2.54 cms, circulation = -1.215 m2/sec, peak vorticity = -67317 sec-1

Figure 22 (continued) - Velocity and streamwise vorticity results for airfoil pairs shedding counter-rotating down vortices.

Figure 23 - The variation of circulation and peak vorticity versus airfoil angle-of-attack alpha, with span-to-boundary layer thickness and airfoil aspect ratio held constant.
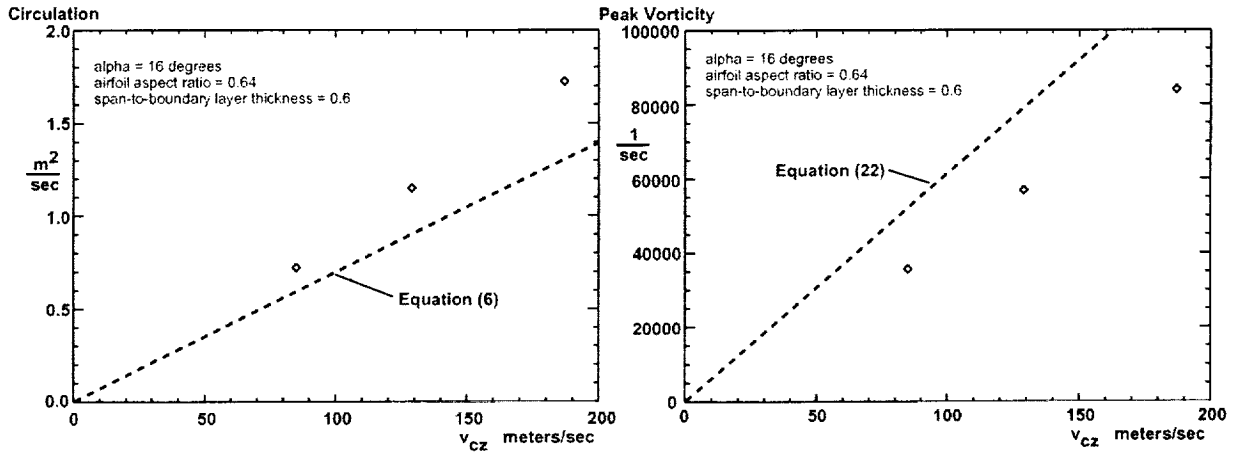
Figure 24 - The variation of circulation and peak vorticity versus pipe core velocity, with airfoil aspect ratio held constant.
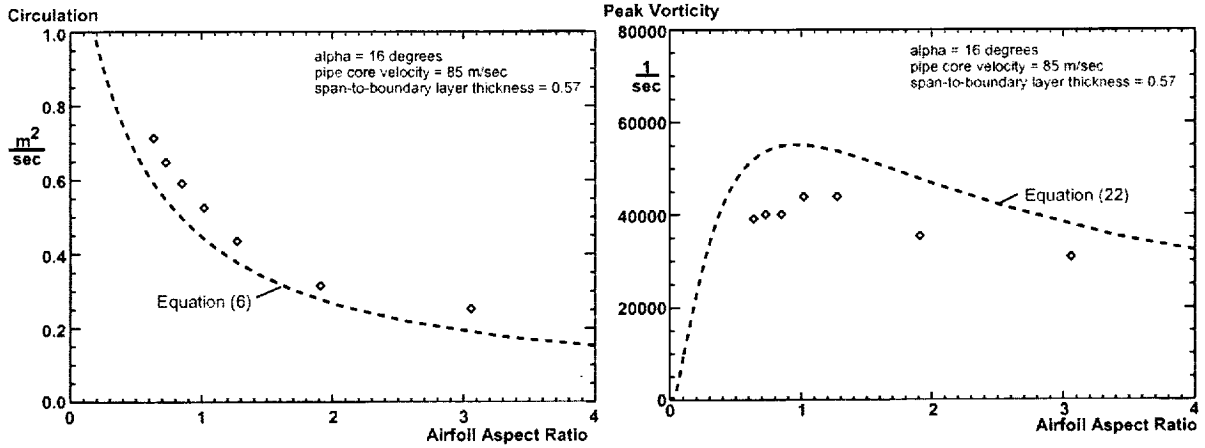

Figure 25 - The variation of circulation and peak vorticity versus airfoil aspect ratio, with span-to-boundary layer thickness held constant.
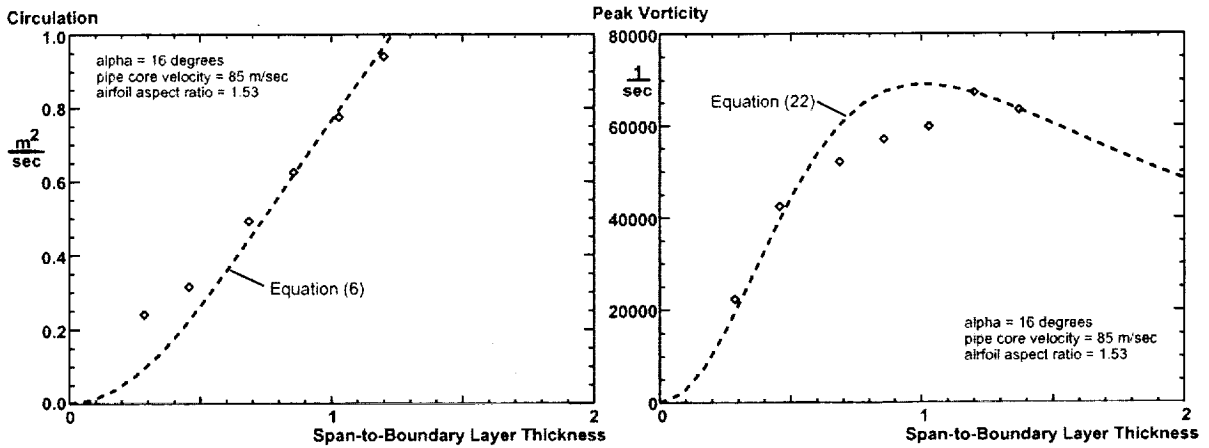

Figure 26 - The variation of circulation and peak vorticity versus span-to-boundary layer thickness ratio, with airfoil aspect ratio held constant.
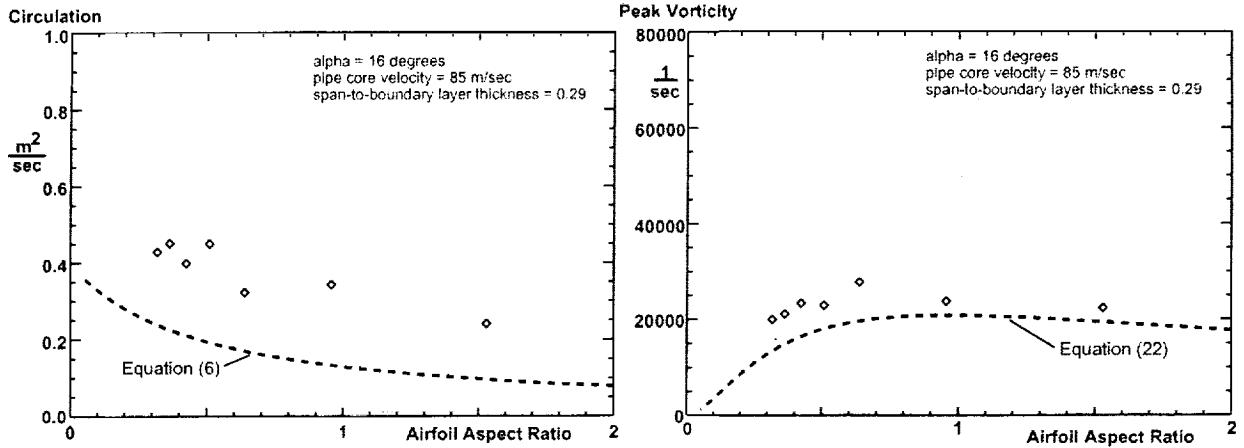
Figure 27 - The variation of circulation and peak vorticity versus airfoil aspect ratio, with span-to-boundary layer thickness held constant.
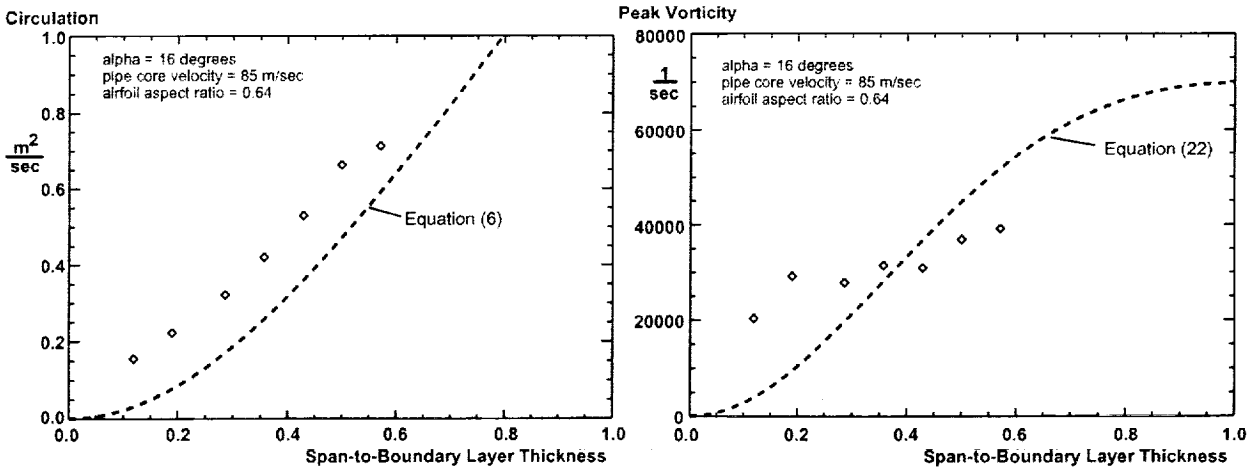

Figure 28 - The variation of circulation and peak vorticity versus span-to-boundary layer thickness ratio, with airfoil aspect ratio held constant.
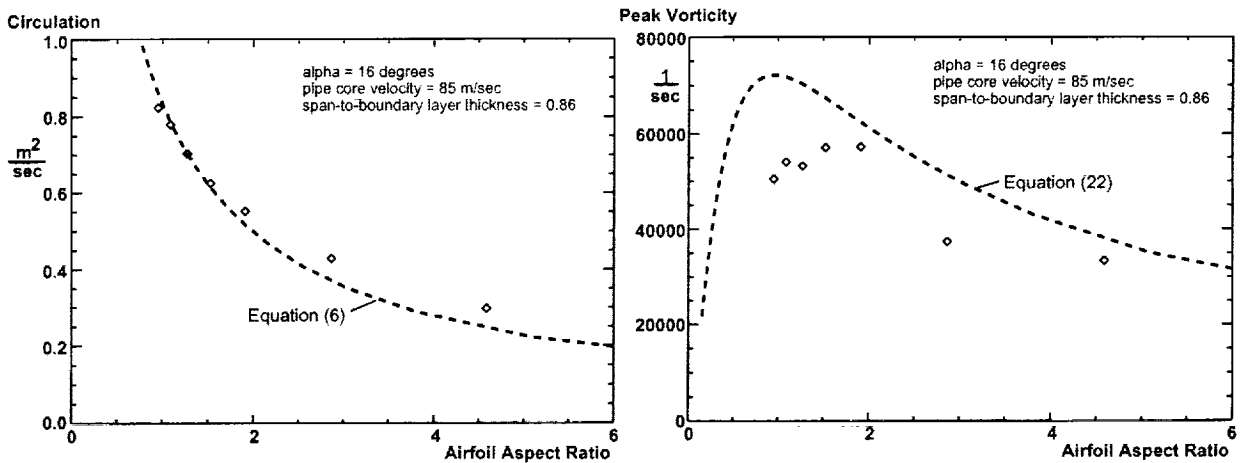

Figure 29 - The variation of circulation and peak vorticity versus airfoil aspect ratio, with span-to-boundary layer thickness held constant.
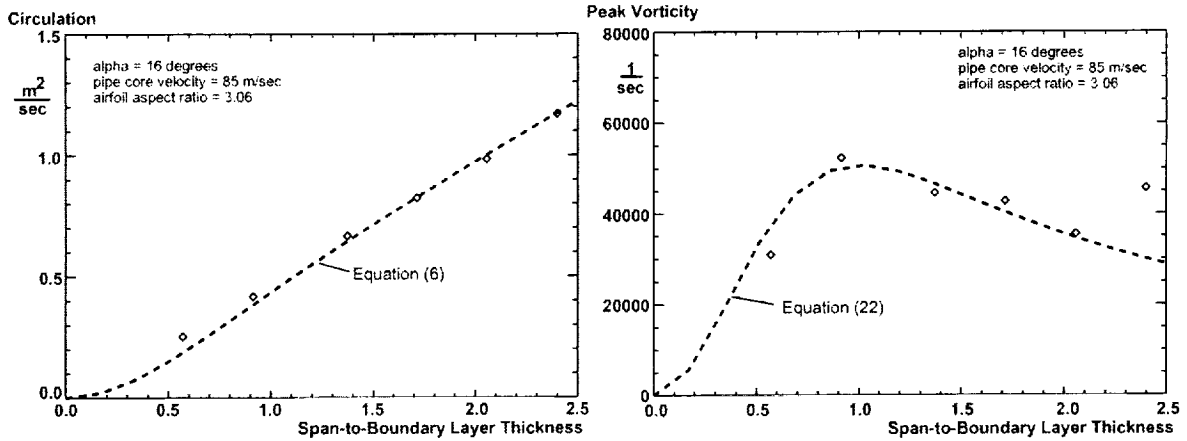
Figure 30 - The variation of circulation and peak vorticity versus span-to-boundary layer thickness ratio, with airfoil aspect ratio held constant.
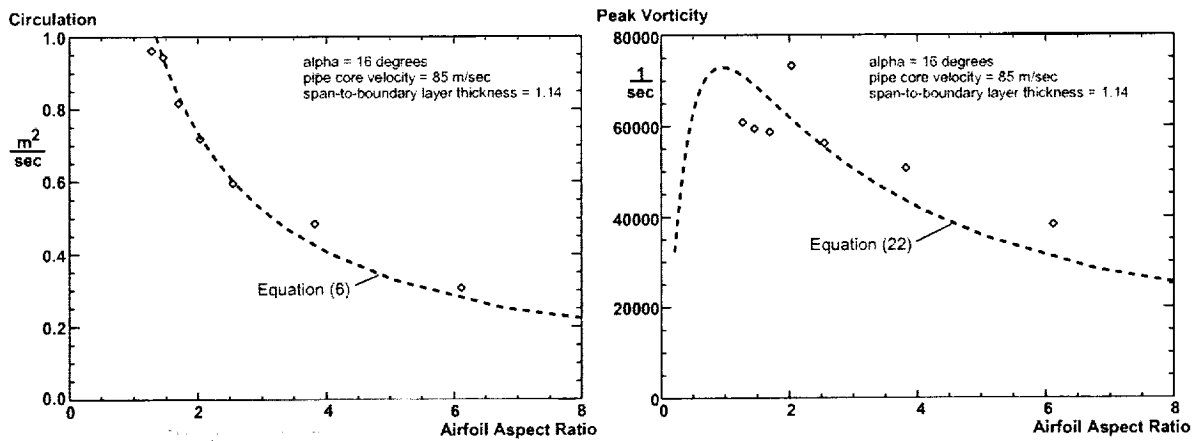

Figure 31 - The variation of circulation and peak vorticity versus airfoil aspect ratio, with span-to-boundary layer thickness held constant.
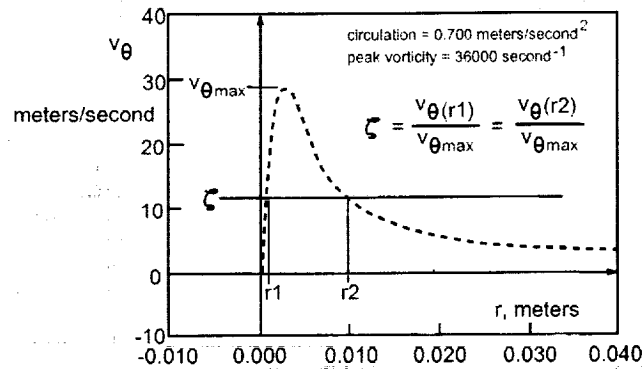

Figure 32 - A plot of angular velocity versus radial location for a Lamb vortex with given descriptors (dashed line). The velocity ratio ζ is realized at both r1 and r2.

REPORT DOCUMENTATION PAGE

Public reporting burden for this collection of information is estimated to average 1 hour per response, including the time for reviewing instructions, searching existing data sources, gathering and maintaining the data needed, and completing and reviewing the collection of information. Send comments regarding this burden estimate or any other aspect of this collection of information, including suggestions for reducing this burden, to Washington Headquarters Services, Directorate for Information Operations and Reports, 1215 Jefferson Davis Highway, Suite 1204, Arlington, VA 22202-4302, and to the Office of Management and Budget, Paperwork Reduction Project (0704-0188), Washington, DC 20503.

1. AGENCY USE ONLY (Leave blank)	2. REPORT DATE August 2001	3. REPORT TYPE AND DATES COVERED Final Contractor Report

4. TITLE AND SUBTITLE Initial Circulation and Peak Vorticity Behavior of Vortices Shed From Airfoil Vortex Generators	5. FUNDING NUMBERS WU-708-73-10-00 NAS3-99138
6. AUTHOR(S) Bruce J. Wendt	

7. PERFORMING ORGANIZATION NAME(S) AND ADDRESS(ES) Modern Technologies Corporation 7530 Lucerne Drive Islander Two, Suite 206 Middleburg Heights, Ohio 44130	8. PERFORMING ORGANIZATION REPORT NUMBER E-12996

9. SPONSORING/MONITORING AGENCY NAME(S) AND ADDRESS(ES) National Aeronautics and Space Administration Washington, DC 20546-0001	10. SPONSORING/MONITORING AGENCY REPORT NUMBER NASA CR—2001-211144

11. SUPPLEMENTARY NOTES

Project Manager, Tom Biesiadny, Turbomachinery and Propulsion Systems Division, NASA Glenn Research Center, organization code 5850, 216-433-3967.

12a. DISTRIBUTION/AVAILABILITY STATEMENT Unclassified - Unlimited Subject Category: 02 Distribution: Nonstandard Available electronically at http://gltrs.grc.nasa.gov/GLTRS This publication is available from the NASA Center for AeroSpace Information, 301-621-0390.	12b. DISTRIBUTION CODE

13. ABSTRACT (Maximum 200 words)

An extensive parametric study of vortices shed from airfoil vortex generators has been conducted to determine the dependence of initial vortex circulation and peak vorticity on elements of the airfoil geometry and impinging flow conditions. These elements include the airfoil angle-of-attack, chord-length, span, aspect ratio, local boundary layer thickness, and free-stream Mach number. In addition, the influence of airfoil-to-airfoil spacing on the circulation and peak vorticity has been examined for pairs of co-rotating and counter-rotating vortices. The vortex generators were symmetric airfoils having a NACA-0012 cross-sectional profile. These airfoils were mounted either in isolation, or in pairs, on the surface of a straight pipe. The turbulent boundary layer thickness to pipe radius ratio was about 17 percent. The circulation and peak vorticity data were derived from cross-plane velocity measurements acquired with a seven-hole probe at one chord-length downstream of the airfoil trailing edge location. The circulation is observed to be proportional to the free-stream Mach number, the angle-of-attack, and the span-to-boundary layer thickness ratio. With these parameters held constant, the circulation is observed to fall off in monotonic fashion with increasing airfoil aspect ratio. The peak vorticity is also observed to be proportional to the free-stream Mach number, the airfoil angle-of-attack, and the span-to-boundary layer thickness ratio. Unlike circulation, however, the peak vorticity is observed to increase with increasing aspect ratio, reaching a peak value at an aspect ratio of about 2.0 before falling off again at higher values of aspect ratio. Co-rotating vortices shed from closely-spaced pairs of airfoils have values of circulation and peak vorticity under those values found for vortices shed from isolated airfoils of the same geometry. Conversely, counter-rotating vortices show enhanced values of circulation and peak vorticity when compared to values obtained in isolation. The circulation may be accurately modeled with an expression based on Prandtl's relationship between finite airfoil circulation and airfoil geometry. A correlation for the peak vorticity has been derived from a conservation relationship equating the moment at the airfoil tip to the rate of angular momentum production of the shed vortex, modeled as a Lamb (ideal viscous) vortex. This technique provides excellent qualitative agreement to the observed behavior of peak vorticity for low aspect ratio airfoils typically used as vortex generators.

14. SUBJECT TERMS Vortices; Vortex generators; Three-dimensional boundary layer	15. NUMBER OF PAGES 49
	16. PRICE CODE

17. SECURITY CLASSIFICATION OF REPORT Unclassified	18. SECURITY CLASSIFICATION OF THIS PAGE Unclassified	19. SECURITY CLASSIFICATION OF ABSTRACT Unclassified	20. LIMITATION OF ABSTRACT

NSN 7540-01-280-5500